



HAL
open science

Unraveling the climate control on debris-free glacier evolution in the Everest region (Nepal, central Himalaya) during the Holocene

Vincent Jomelli, Patrick Wagnon, Didier Swingedouw, Joanna Charton, Régis Braucher, Adèle Hue, Fanny Brun, Christophe Colin, Stephanie Gairoard, Dibas Shrestha, et al.

► To cite this version:

Vincent Jomelli, Patrick Wagnon, Didier Swingedouw, Joanna Charton, Régis Braucher, et al.. Unraveling the climate control on debris-free glacier evolution in the Everest region (Nepal, central Himalaya) during the Holocene. *Quaternary Science Reviews*, 2023, 310, pp.108109. 10.1016/j.quascirev.2023.108109 . hal-04097595

HAL Id: hal-04097595

<https://hal.science/hal-04097595>

Submitted on 15 May 2023

HAL is a multi-disciplinary open access archive for the deposit and dissemination of scientific research documents, whether they are published or not. The documents may come from teaching and research institutions in France or abroad, or from public or private research centers.

L'archive ouverte pluridisciplinaire **HAL**, est destinée au dépôt et à la diffusion de documents scientifiques de niveau recherche, publiés ou non, émanant des établissements d'enseignement et de recherche français ou étrangers, des laboratoires publics ou privés.

- Holocene glacier fluctuations in Himalaya remain puzzling
- We investigate the evolution of two debris-free glaciers in the Everest region
- Glacier chronologies are based on 51 ^{10}Be ages from moraines and roche moutonnees
- The two glaciers show their largest Holocene extent in the Early Holocene.
- We do not observe any moraine from the Mid-Holocene
- Several minor advances are recorded during the Late Holocene
- This pattern does not perfectly conform current knowledge on Asian monsoon changes

1 Unraveling the climate control on debris-free glacier evolution in the Everest region (Nepal,
2 Central Himalaya) during the Holocene

3

4 Vincent Jomelli* Patrick Wagnon², Didier Swingedouw³, Joanna Charton¹, Régis Braucher¹,
5 Adèle Hue¹, Fanny Brun², Christophe Colin⁴, Stephanie Gairoard¹, Dibas Shrestha⁵, Aster
6 TEAM*

7

8 1. Aix-Marseille University, CNRS, IRD, Coll. France, INRAE, CEREGE, 13545 Aix-
9 en-Provence. France, * corresponding author jomelli@cerege.fr

10 2. Univ. Grenoble Alpes, CNRS, IRD, INRAE, IGE, F-38000 Grenoble, France

11 3. Environnements et Paléoenvironnements Océaniques et Continentaux (EPOC),
12 UMR CNRS 5805, EPOC-OASU Université de Bordeaux, Allée Geoffroy
13 Saint-Hilaire, 33615 Pessac, France

14 4. Université Paris-Saclay, CNRS, GEOPS, 91405, Orsay, France

15 5. Central Department of Hydrology and Meteorology, Tribhuvan University,
16 Kathmandu, Nepal

17

18 *Aster Team members: Georges Aumaître, Karim Keddadouche, Fawzi Zaidi

19 Keywords: Nepalese glacier, 10Be chronology, Holocene, AMOC, Indian monsoon.

20

21 Abstract

22 Current mass balance and meteorological surveys of Mera glacier located about 30 km south of
23 Mount Everest in Nepal show the dominant role of Asian monsoon precipitation on interannual
24 mass balance variability while temperature controls the altitude of snow-rain threshold. As

25 these observations on mass balance variability only explore the recent decades, studies on paleo
26 glacial extents are useful to investigate the long-term climate forcing on glacier evolution. To
27 do so, we investigated the long-term evolution of the debris-free Mera glacier and a
28 neighbouring small debris-free South Khare glacier. Fifty-one ^{10}Be CRE ages were obtained
29 from samples collected on moraine boulders and roches moutonnées. ^{10}Be CRE ages of the
30 boulders span from the end of the Lateglacial (19.0 – 11.7 ka) to the Little Ice Age (~ 0.6-0.1
31 ka). The oldest dated moraine in this study was observed at the base of South Khare glacier
32 with an age of 13.6 ± 0.5 ka. The two glaciers subsequently experienced their largest Holocene
33 extent in the Early Holocene with moraines dated to 11.0 ± 0.3 ka at the base of Mera glacier
34 and 10.8 ± 0.5 ka at the base of South Khare glacier. We did not observe any moraine from the
35 Mid-Holocene. During the Late Holocene several glacier advances were recorded around $2.3 \pm$
36 0.2 ka, 1.5 ka and then during the last centuries at Mera glacier and around 2.8 ± 0.6 ka, and
37 during the Little Ice Age at South Khare glacier. To explore the links between long-term
38 Nepalese glacier changes and climate, we used oceanic and terrestrial Indian Summer monsoon
39 reconstructions and temperature and precipitation output from two transient global climate
40 models TraCE and LOVECLIM. These climate data outputs were corrected by a reconstruction
41 of the Atlantic Meridional Overturning Circulation (AMOC) over the Holocene and its
42 associated climatic impacts. We also used sensitivity experiments from the IPSL (Institut Pierre
43 Simon Laplace) model to discuss the possible influence of horizontal resolution, land
44 hydrology, vegetation and runoff on changes in Asian summer monsoon. Importantly, we show
45 this long-term Nepalese glacier pattern does not perfectly conform neither to the Indian
46 monsoon precipitation that is documented from terrestrial and marine records nor to
47 temperature and precipitation changes simulated by the models. While the maximum glacier
48 extent in the Early Holocene corresponds to enhanced precipitation documented by proxies and
49 models, the Late Holocene glacier advance remains puzzling. We claim that new paleo glacier

50 records and improved climate simulations are necessary to get a better understanding of past
51 glacier changes and the associated climate dynamics, which might be crucial to gain confidence
52 in both glacier and climate future evolutions.

53

54 1-Introduction

55 Over the last decades the recent evolution of the High Mountain Asian (HMA) glaciers mass
56 balance has been widely investigated as they contribute importantly to water resources for
57 approximately 800 million people and are a component of global sea level rise (Brun et al.,
58 2017; Pritchard, 2019; Azam et al., 2021). Recent studies covering most HMA glaciers have
59 revealed an overall mass loss over the last decades with values about -0.18 ± 0.04 m of water
60 equivalent per year (w.e. yr^{-1}) with strong spatial and individual glacier mass balance
61 variability (Brun et al 2017; Hugonnet et al., 2021).

62 This large spatio-temporal mass balance variability is mainly due to climate and
63 geomorphological causes. Along the HMA temperature and precipitation vary spatially and
64 temporally, leading to heterogeneous climate change and behavior of glaciers (e.g., Sakaï and
65 Fujita 2017; Yan et al., 2018, 2020; Azam et al., 2021). In addition, Sakaï and Fujita (2017)
66 evidenced a spatially variable sensitivity of mass balances of HMA glaciers to temperature
67 while their behavior also depends on precipitation changes.

68 The other main cause of mass balance variability is related to the geomorphological context of
69 individual glaciers. Brun et al. (2019) have reported that the slope of the glacier tongue, the
70 mean glacier elevation, the percentage of supraglacial debris cover, the avalanche contributing
71 area and the presence of a lake at the base of glaciers all together explain between 11 and 48%
72 of the current mass balance variability.

73 However, as these contributions only explore the recent decades, studies on paleo glacial
74 extents during the Holocene and older periods are needed to investigate potential influence of

75 long-term climate forcing on multi-centennial to millennial glacier evolution and thus offer an
76 opportunity to put the recent glacier decline in a longer perspective.

77 Previous studies that investigated glacier fluctuations during the Lateglacial and the Holocene
78 (11.7 ka - present) using *in situ* produced ^{10}Be cosmic ray exposure (CRE) ages have shown that
79 the multi-centennial glacier evolution differs across the HMA.

80 This is assumed to reflect the spatial variability of precipitation and temperature as currently
81 observed. This is related to relative influence of the mid-latitude westerlies, the Indian Summer
82 Monsoon (ISM) and the East Asian Summer Monsoon (ESM) (Owen et al., 2008, 2009; Owen,
83 2009; Owen and Dortch, 2014; Saha et al., 2019). While the mid-latitude westerlies might
84 significantly influence the western end of the range and Tibet (Mölg et al., 2014), the ISM and
85 ESM both combined in the Asian Summer Monsoon are believed to largely dominate the
86 southern and eastern regions, and to a lesser extent the interior (continental) portions of the
87 HMA.

88 As it is observed that the geomorphological context has influence on mass balance variability
89 over the current period, this geomorphological context should also be considered while
90 investigating long-term glacier change. For instance, in the Khumbu valley, (Everest region,
91 Nepal) previous studies of glacier fluctuations from the Lateglacial were conducted on large
92 debris-covered glaciers (Finkel et al., 2003; Hornsey et al., 2022). However, a detailed
93 understanding of the Lateglacial-Holocene glacier history from debris-free glaciers in the
94 central Himalaya is lacking (Saha et al., 2019). Thus it remains still unclear if the debris cover
95 in the ablation zone may have influenced the long-term glacier response to climate change
96 compared to debris-free glaciers (Owen et al., 2005).

97 In this context we investigated the fluctuations of two debris-free glaciers in Nepal (Everest
98 region (Fig.1)), based on 51 ^{10}Be CRE ages determined from rock samples of moraine boulders
99 (n=43) and roche moutonnées (n=8) whose ages span the Lateglacial and the Holocene. The

100 main goals of this study are to document major periods of advances of these two glaciers at a
101 multi-centennial time scale during the Holocene, to compare this signal with other glaciers in
102 Nepal and investigate the potential long-term climate forcings responsible for their evolution.
103 Among the two investigated glaciers, the Mera glacier is an ideal target to explore long-term
104 glacier-climate relationship and compare long-term vs. short-term glacier response to climate
105 change. Indeed, on this glacier an understanding of physical processes driving current mass
106 balance has been led through mass and energy balances surveys since 2007 (Wagon et al.,
107 2013; 2021; Sherpa et al., 2017; Litt et al., 2019). The originality of this study is thus to combine
108 different approaches i.e., surface process understanding at present, as well as moraine dating,
109 climate reconstructions and climate model outputs over the Lateglacial-Holocene period, to
110 unravel the climate control on debris-free glacier evolution in the Everest region. The study
111 area, moraine stratigraphy and the climate setting are presented in section 2. Based on the
112 methodology described in section 3, CRE moraine ages are presented in section 4. In section 5-
113 1, 5-2 and 5-3 we discuss our moraine records and compare the two chronologies with other
114 studies conducted in Nepal and in other regions of HMA respectively. In section 5-4 we discuss
115 potential forcings driving the evolution of the two investigated glaciers.

116

117 2- Study Area and climate setting

118 2-1 Physical setting

119 The two investigated Mera (ME) and South Khare (SK) glaciers are located in the upper Dudh
120 Koshi basin, at about 30 km south of Everest summit (central Himalaya, 27°.74 Lat; 86°.86
121 Long) (Fig. 1). In this area the bedrock is dominated by quartz-rich granite and gneiss. Mera
122 glacier is a debris-free summer-accumulation glacier type with an area of 4.84 ± 0.34 km² in
123 2018 and a maximum altitude of 6420 m a.s.l. (Wagon et al., 2021). The glacier extends
124 northwards and divides into two branches at 5800 m a.s.l.. The main branch, oriented north-

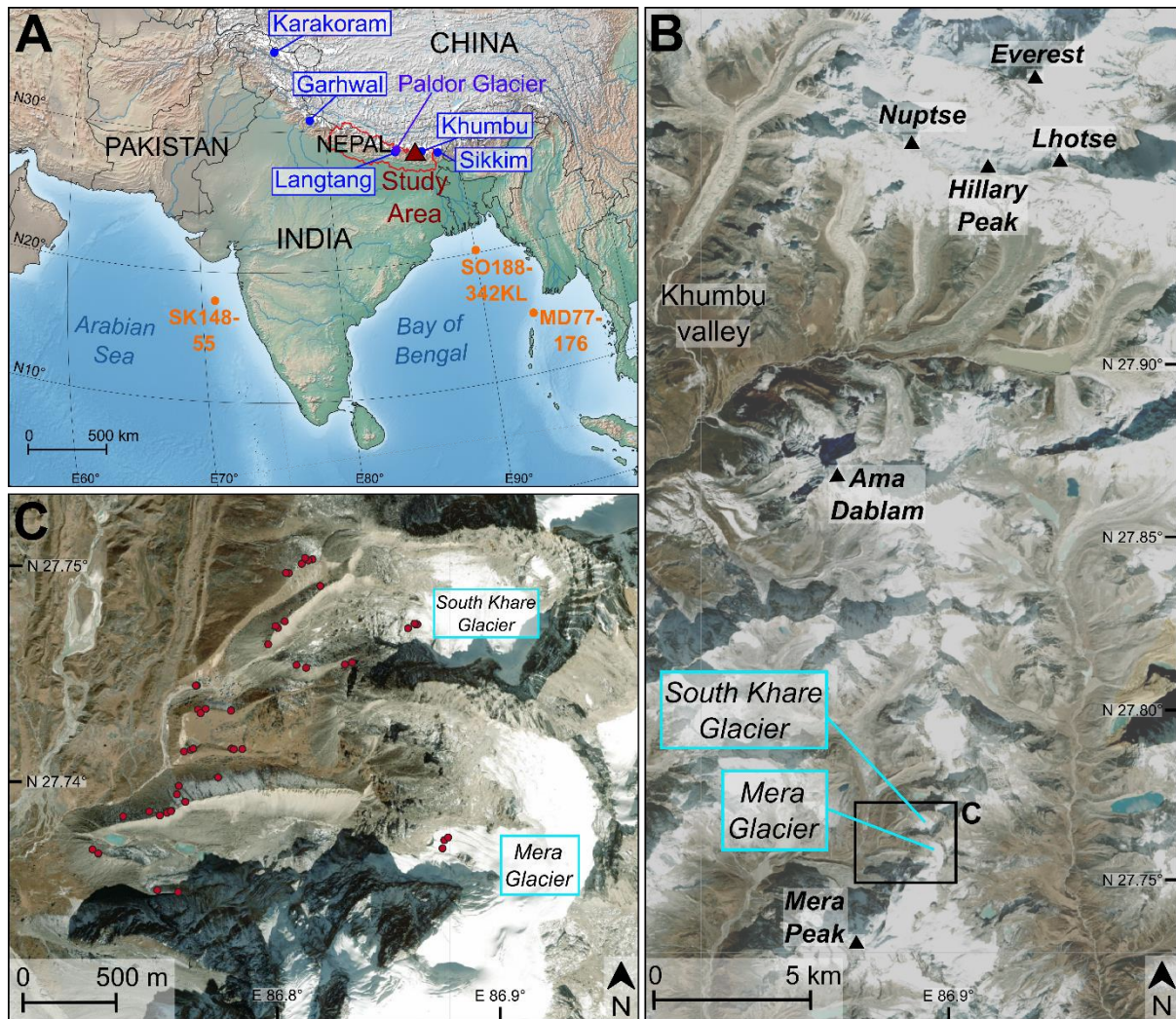
125 west, with a mean slope of $\sim 16^\circ$, goes down to 4910 m a.s.l. at snout. Here, samples from
126 several moraines were collected. The minor Naulek branch, oriented north-east was not
127 investigated in this study. Mera glacier mass balance has been investigated both using the
128 classical glaciological (stakes) method since 2007 and more recently the geodetic method
129 (Wagnon et al., 2013; 2021). Annual and seasonal measurements of the glacier mass balance
130 showed that the accumulation and ablation processes happen during the same monsoon period.
131 There is limited mass change during the dry, cold and windy winter, apart from wind ablation
132 and sublimation (Sherpa et al., 2017; Litt et al., 2019; Wagnon et al., 2021). The glacier-wide
133 mass balance calibrated over geodetic mass balance was slightly negative for the period 2007-
134 2013 (MB -0.23 ± 0.23 m w.e./yr) with more negative values for the period 2013-2020 (-0.57
135 ± 0.19 m w.e./yr) (Wagnon et al., 2021). In addition the mass balance variations of this glacier
136 are in agreement with observations conducted at a regional scale (Hugonnet et al 2021). Thus,
137 it can be seen as representative of the regional trend. Mera glacier is bounded by six distinct
138 lateral moraines, which were named, from the right to the left side of the glacier looking
139 downhill, M1 for the youngest to M₆ for the oldest i.e. Mera ME-M1 to M6 (Figs. 2, 3). A large
140 terminal moraine over 200 m wide formed by the nested crests (ME-M1, -M2, -M3), is cut by
141 a small river from the glacier with a frontal ramp 50 m in relief (Figs 2, 3). On the right side of
142 the Mera glacier about 400 m downstream from the front and about 200 m below in altitude,
143 two large lateral moraines are visible. The inner one is composed of the three nested ridges
144 (ME-M1, -M2, -M3). The ME-M1 lateral moraine is continuous over about 1.5 km from the
145 terminus and is actually superimposed on two other lateral moraines ME-M2 and ME-M3 and
146 certainly explains its large relief. The ME-M1 moraine has unvegetated or poorly vegetated
147 surfaces and unstable proximal slopes with crest heights up to 80 m above the proglacial sandur
148 formed by the river flowing from the front of the glacier. The Mera ME-M2 and ME-M3 right
149 lateral moraines are fragmented and only identifiable from 200 m and 500 m respectively up-

150 glacier from the terminus. Both crests are separated by 10–50 m horizontally from the Mera
151 moraine ME-M1 and at a lower altitude (30 and 50 m respectively). The distal slope of these
152 two moraines is steep but stable and vegetated. The relief of these two ridges is not well
153 developed and generally does not exceed 3 m in height.

154 Distant to about 200 m from the rampart towards the north, separated by approximately 50 m
155 horizontally from ME-M3, an older lateral moraine (ME-M4) is totally covered by vegetation.
156 This lateral moraine shows two distinct crests and only the distal one has been investigated.
157 This right lateral ME-M4 moraine has an asymmetrical cross-profile with a rather flat surface
158 and a steep but stable, vegetated distal slope (Figs 2, 3).

159 Downslope the moraine ME-M4 was probably connected to the lateral moraine of South Khare
160 glacier. The crest is rounded and has a relief of about 20 m above the valley floor. Moraines on
161 the left side of the glacier are less well preserved. Only two ridges were investigated. One is
162 relatively fresh in shape (ME-M5) while the other (ME-M6) is also covered by vegetation. From
163 the terminus of the frontal moraine a fragmented ridge is only identifiable over about 100 m
164 toward the glacier. At an altitude of about 4750 m a.s.l. the ridge of ME-M5 is buried by another
165 moraine which was not studied. This part of the left side of the glacier was also impacted by
166 dirty snow avalanches and was not deeper investigated. The relief of this left lateral moraine
167 ME-M5 is about 50 m above the valley. ME-M6 moraine is only preserved from periglacial
168 processes over a distance of approximately 100 m. This vegetated moraine constitutes the most
169 external ridge of the rampart on the left side of the glacier. On the inner side of these two
170 moraines, several ridges are visible but are too steep to be sampled.

171



172

173

174 **Figure 1.** Location map of Mera and South Khare glaciers (blue frames) and other relevant
 175 locations presented throughout the study (black triangles correspond to the summits) in the
 176 upper Dudh Koshi basin, Everest region (central Himalaya). a). The inset shows the study area
 177 (red triangle) in the High Mountain Asia. Blue dots correspond to the different regions of the
 178 HMA, the purple dot shows another glacier cited in this study and orange dots show the location
 179 of marine cores discussed in the text. b). Debris free and debris-covered discussed in this study.
 180 **c). Mera and South Khare moraine records with sample locations (red dots).**

181

182 South Khare glacier (0.47 km²) is located 1 km north of Mera glacier and has a catchment area
 183 of ~2.7 km² with an elevation ranging from ~5200 m a.s.l at the front to ~5890 m a.s.l at the

184 top (Fig. 1). It is also a debris-free glacier facing west with a mean slope of $\sim 17^\circ$. At the base
185 of South Khare glacier, the configuration of the moraines is rather similar to that of Mera glacier
186 with eight identified moraines the SK M1–8 moraines, with each crest separated by 2–70 m
187 horizontally (Figs. 4, 5). At a distance of ~ 700 m down-valley from the current front position,
188 a large rampart of about 60 m high is composed of at least two young nested lateral moraines
189 with individual crests (SK-M1, -M2 on the right side, -M6, -M7 on the left side) that were
190 sampled at both sides of the valley. The South Khare right lateral moraine SK-M1 is continuous
191 along the right of the glacier with an elevation ranging from 5010 to 5200 m a.s.l.
192 Down-valley of the right side of the glacier, two distinct crests (SK-M3, -M5) were
193 investigated. The youngest crest forms a continuous right lateral moraine SK-M3 of about 300
194 m in length. The relief of this lateral moraine exceeds 50 m. The steep proximal slope is
195 dissected by relict and active gullies while the distal slope shows only very few boulders with
196 a sub horizontal surface. A remnant ridge SK-M5 of 2 m in relief on the right side of the glacier
197 is distant to about 10 m from SK-M3 horizontally. This discontinuous ridge is only visible near
198 the ablation zone while downslope the crest connected to the lateral moraine SK-M4 disappears.
199 On the left side of the glacier two crests are also visible on the upper part of the ablation area
200 close to each other horizontally The uppermost ridge SK-M6 forms a continuous crest of about
201 50 m in relief with a symmetric cross profile. The altitude of this ridge between 5000 and 5150
202 is the same as SK-M1 on the right side of the glacier. This moraine is up to 80 m in relief
203 dominating the village of Khare. On the distal slope of the ridge another discontinuous crest
204 SK-M7 is visible at about 5040 m a.s.l. over a distance of 50 m. Approximately 150 m
205 horizontally towards the south from SK-M7 an old vegetated and rounded moraine SK-M8 of
206 about 30-50 m in relief is visible.

207

208

209

210 2-2 Climate Setting

211 The Everest region is under the influence of the ISM, when approximately three quarters of the
212 annual precipitation fall during the summer months from June to September (Litt et al., 2019;
213 Perry et al., 2020). For the year 2019-2020, the Northern Bay of Bengal is the most important
214 source of moisture during the monsoon (62 %), more than from the Indus River Delta and
215 Arabian Sea (21 %) and Indo-Gangetic Plain (17%) (Perry et al., 2020). From October to May,
216 the westerlies on the continent are predominant for precipitation (Perry et al., 2020). The
217 monsoon usually stops suddenly at the end of September/beginning of October when the
218 weather, mostly cloudy, calm and warm with frequent precipitation switches within a few days
219 to constantly sunny and dry conditions, progressively colder and windier, during the post
220 monsoon (October-November). Very dry, sunny and windy conditions prevail during the winter
221 (December - February) where there is almost neither any clouds nor precipitation. From March
222 to May, the pre-monsoon is characterized by a progressive increase in convective clouds
223 bringing warm and humid air, with progressively more and more precipitation and a decrease
224 in strong winds (Bookhagen and Burbank, 2006; Sherpa et al., 2017; Khadka et al., 2021).

225

226 2-3 Processes controlling the glacier mass balance

227 In this Indian monsoon-dominated region, over **debris-free** glaciers, ablation is dominated by
228 melt in the lower part of the glacier **below** the equilibrium line altitude (ELA) above which
229 sublimation plays a substantial role during all seasons, except the monsoon (e.g. Wagnon et al,
230 2013; Stigter et al., 2018; Litt et al., 2019; Fugger et al., 2022). The radiation budget mostly
231 controls the melt (Stigter et al., 2021). The incoming shortwave radiation is maximal during the
232 pre-monsoon, before the installation of permanently overcast conditions during the monsoon,
233 responsible for maximal incoming longwave radiation compensating the heat loss *via* outgoing

234 longwave radiation (Bonekamp et al, 2019; Matthews et al, 2020). Overall, the net all-wave
235 radiation is high during the pre-monsoon and monsoon and is controlled by the albedo and by
236 the seasonality of cloudiness (the percentage of cloud in a given atmospheric layer) (Bonekamp
237 et al., 2019; Stigter et al., 2021). Snow with its impact on albedo and air temperature and its
238 control on the rain-snow limit, are therefore very important meteorological variables
239 influencing the glacier mass balance in the ablation area. Wind speed, which governs
240 sublimation, is more important in the accumulation area. Most of the ablation still happens
241 during the monsoon due to stronger melt than during the pre-monsoon season, when refreezing
242 compensates the melt until the cold content of the glacier surface layers originating from the
243 winter has been evacuated (e.g., Fugger et al., 2022).

244

245 3- Methods

246 3-1 Field sampling

247 The field campaigns took place in 2014, 2016 and 2018. Moraines were sampled and mapped
248 in the field using a Garmin GPS survey instrument (precision 10 m) (Table 1). Using a hammer
249 and a chisel, 51 granitic boulders (> 60 cm in height) were sampled from the crest of the 14
250 selected moraines and on roches moutonnées (bedrock) close to the front of the glaciers. A
251 Suunto Compass Clinometer PM-5 was used to measure topographic shielding for each sample
252 in the field. Sample elevation was extracted from the handheld Garmin GPS instrument. All the
253 boulders were photographed and their ground-to-sample height was measured. We have
254 considered well-preserved moraines (> 1 m high and > 20 m long), and selected boulders and
255 locations on the moraine with no evidence of disturbance caused by the action of other processes
256 (river, rock fall or debris flow; Jomelli and Francou 2000).

257 In order to document the deglaciation chronology of Mera (ME) and South Khare (SK) glaciers,
258 we first collected samples on roches moutonnées close to their current front position (Figs 2-

259 5). Other samples were collected downslope on lateral moraines at approximately 1-2 km from
260 the current front.

261

262 3-2 Sample preparation and AMS measurement

263 All samples were processed at CEREGE (Aix-en-Provence, France). Samples were crushed and
264 sieved to collect the 250-1000 μm fraction. Quartz was first concentrated by magnetic
265 separation and then isolated by successive leaching in a $\frac{2}{3}$ H_2SiF_6 / $\frac{1}{3}$ HCl mixture. The
266 obtained quartz fraction was leached at least 3 times in a 10% HF - 10% HNO_3 solution, in order
267 to remove any remaining feldspars and to clean the grains from atmospheric ^{10}Be . Purified quartz
268 was completely dissolved in concentrated HF (48%) after addition of an in-house ^9Be carrier
269 solution (3025 ± 9 ppm; Merchel et al., 2008). Beryllium was extracted by successive alkaline
270 precipitations of $\text{Be}(\text{OH})_2$ alternated with separation on anion and cation columns. Samples
271 were then oxidized at 700°C for 1 hour and the final BeO mixed with Nb powder and loaded
272 into copper cathodes. AMS measurements of the $^{10}\text{Be}/^9\text{Be}$ ratios were conducted at the French
273 national AMS facility ASTER (Arnold et al., 2010). Samples were calibrated against the in-
274 house standard STD-11 ($^{10}\text{Be}/^9\text{Be} = 1.191 \pm 0.013 \cdot 10^{-11}$; Braucher et al., 2015) and a ^{10}Be half-
275 life of $1.387 \pm 0.0012 \cdot 10^6$ years (Chmeleff et al., 2010; Korschinek et al., 2010). Analytical
276 uncertainties combine ASTER counting statistics, standard uncertainty, external uncertainty
277 (0.5%; Arnold et al., 2010) and machine blank correction. ^{10}Be concentration in the sample was
278 calculated from the corresponding $^{10}\text{Be}/^9\text{Be}$ ratio and was corrected from associated chemical
279 blanks (Table 1). Scaling to the sample locations was made according to the recent, physically-
280 based, LSD model (Lifton et al., 2014) which performs similarly to older empirical models
281 presented in Borchers et al., (2016). Chosen parameters include the ERA 40 atmospheric
282 reanalysis (Uppala et al., 2005) and the VDM 2016 geomagnetic database. We used the SLHL

283 global production rate of 4.08 ± 0.23 atoms $\text{g}^{-1} \text{yr}^{-1}$ as no regional production rate is available so
284 far.

285 Exposure ages were computed with the online CREp program (Martin et al., 2017;
286 <http://crep.cirp.cnr-nancy.fr>) and are presented in Table 1. In order to make our results easily
287 comparable to previous studies carried out in other regions of the HMA, we present in Table 2
288 the exposure ages computed using the time-dependent “Lm” scaling model (Lal, 1991; Stone,
289 2000) and recalibrated previous data when comparisons were made with previous studies.

290 ^{10}Be CRE ages are reported with 1σ “external” uncertainties, which include measurement,
291 production rate and scaling uncertainties (e.g., Balco et al., 2008), in the main text and on the
292 maps (Figs. 2, 4) for better comparison with other proxies. Both internal and external
293 uncertainties are reported in Table 1. For comparison we have recalculated all moraine ages
294 using the different tests such as Chevenet’s and Peirce’s referenced in Batbaatar et al. (2018)
295 that are summarized in the table S1. However, for a given moraine, its assigned age corresponds
296 to the weighted mean of the sample ages that successfully passed a Chi^2 test (calculated with
297 the internal uncertainties) used to identify outliers (Ward and Wilson, 1978). Chi^2 test was
298 preferred because it is the most conservative test compared to the others (see Table 1). Based
299 on field observations, we also considered the stratigraphic relationships to identify outliers.

300

301 3-3 Paleoclimate data from the two transient model simulations

302 To explore links between glacier behavior and climate forcings we have used output from two
303 available transient global climate model (GCM) simulations from LOVECLIM (Kobashi et al.,
304 2016) and CCSM4 (Liu et al., 2009). The so-called TraCE simulation from CCSM4 includes
305 variations in insolation, greenhouse gas concentrations, ice sheet extension and altitude from
306 the ICE5-G reconstruction and also a crude estimate of associated freshwater release in the
307 North Atlantic. LOVECLIM uses similar forcings, but ICE-6G for the ice sheet, and does not

308 account for freshwater release in the North Atlantic. This second transient simulation also
309 includes an estimate of volcanic forcing, which is not included in the TraCE simulation.

310 As the Atlantic Meridional Overturning Circulation (AMOC) evolution is poorly represented
311 in the two models, we corrected the transient simulations using the Ayache et al. (2018)
312 reconstruction of the AMOC.

313 The AMOC reconstruction for Ayache et al. (2018) was then calibrated using Northern
314 Hemisphere reconstruction of Kaufman et al. (2020) and transient model simulations as well as
315 hosing simulations from Swingedouw et al. (2013), in order to quantify the climatic impacts of
316 AMOC variations. From there, the variables simulated in the transient run have been corrected
317 using a semi-empirical model described in detail in Jomelli et al. (2022).

318

319 For comparative purposes we also included in our analysis Mid-Holocene to present-day
320 evolution of the ISM from other transient global simulations described in detail in Cretat et al.,
321 (2020). Here we benefited from sensitivity analyses conducted by the authors who investigated
322 the effects of horizontal resolution, land hydrology, vegetation and runoff on changes in the
323 ISM, with a focus on its seasonality at the monthly time scale and on extremes at the seasonal
324 time scale. They also analyzed changes in the interannual-to-decadal variability of the ISM
325 from two model versions of the IPSL Earth System model.

326

327 3-4 Comparison with other moraine chronologies from the HMA

328 To get a better understanding of glacier fluctuations in the HMA we explored other CRE
329 moraine records from the worldwide Ice-D database (<http://alpine.ice-d.org/>). Here we have
330 applied four criteria to be consistent with the analysis. We did not consider moraines dated with
331 only one CRE age or unpublished data. We focused on glacial valleys without undated moraine
332 that may have been formed during the timeframe investigated in this study. As an example, a

333 study that would provide an age for a Lateglacial moraine without dating other moraines located
334 upstream would not be conclusive for our purpose and thus would not be considered in the
335 regional comparison. In addition, a moraine dated with ages that show a large dispersion is
336 rejected for the same reason as possibly reflecting inheritance or post depositional
337 changes. Following the same strategy, we did not consider glacial valleys with moraines dated
338 with uncertainties that do not make possible to attribute the moraine formation to a specific
339 period (Lateglacial or Early, Mid or Late Holocene).

340

341 4- Results

342 We present 51 ^{10}Be CRE ages in this contribution, 25 ^{10}Be CRE ages from Mera glacier and 26
343 ^{10}Be CRE ages from South Khare glacier.

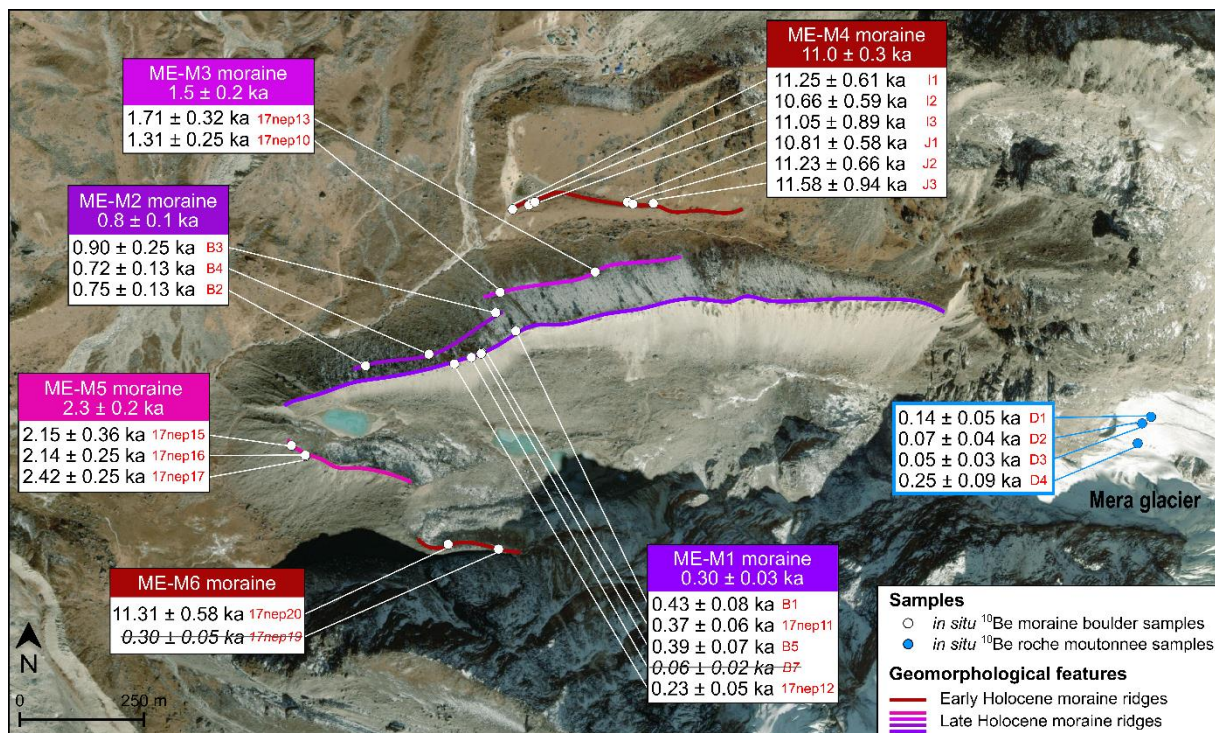
344

345 4-1 Mera glacier chronology

346 The chronology of the Mera glacier is based on samples from roche moutonnées located just a
347 few meters below the current front position of the glacier and from six moraines (Figs. 2, 3).
348 Four samples (D1, D2, D3, D4) were collected on roche moutonnées that were covered by ice
349 until recent years. Apparent CRE ages of these samples range between 0.05 ± 0.03 ka to $0.25 \pm$
350 0.09 ka. As these surfaces were covered by ice and therefore protected from cosmic rays, until
351 recent years (this is evidenced in recent aerial photos and successive field trips during which
352 we witnessed the frontal retreat of the glacier) their apparent ages should be null. The apparent
353 young ages for D1 and D4 are probably due to inheritance due to insufficient resetting by ice
354 abrasion since a potential previous exposure or pre-exposure under reduced ice thickness during
355 the last centuries. Five samples (B1, B5, B7, 17nep11 and 17nep12) were taken on this youngest
356 and highest ridge ME-M1. ^{10}Be CRE ages are between 0.06 ± 0.02 ka (B7) and 0.43 ± 0.08 ka
357 (B1). Among these samples, B7 was considered as an outlier based on Chi^2 test and was

358 excluded from the mean age calculation of the moraine that yields a ^{10}Be CRE age of $0.30 \pm$
 359 0.03 ka ($n=4$). Three samples were collected on the Mera right lateral moraine ME-M2. Here
 360 we selected the largest boulders and tried to avoid boulders that could have fallen from the
 361 moraine ME-M1. These samples B2 (0.75 ± 0.13 ka), B3 (0.90 ± 0.25 ka), and B4 (0.72 ± 0.13
 362 ka) yield a weighted mean ^{10}Be CRE age of 0.8 ± 0.1 ka ($n=3$). On the third nested right lateral
 363 moraine ME-M3, the two samples 17nep10 (1.31 ± 0.25 ka) and 17nep13 (1.71 ± 0.3 ka) yield
 364 a mean ^{10}Be CRE age of 1.5 ± 0.2 ka. The right lateral moraine ME-M4 was dated at 11.0 ± 0.3
 365 ka from the weighted mean of six samples (I1, I2, I3, J1, J2, J3) that showed rather consistent
 366 ^{10}Be CRE ages ranging between 10.7 ± 0.6 ka and 11.6 ± 1 ka. ME-M5 was dated to 2.3 ± 0.2
 367 ka based on three samples (17nep15, 17nep16 and 17nep17). Finally, the older short ridge left
 368 lateral moraine ME-M6 was tentatively dated to 11.3 ± 0.6 ka based on the only sample
 369 17nep20, because 17nep19 age (0.30 ± 0.05 ka) is considered as an outlier based on
 370 stratigraphy.

371

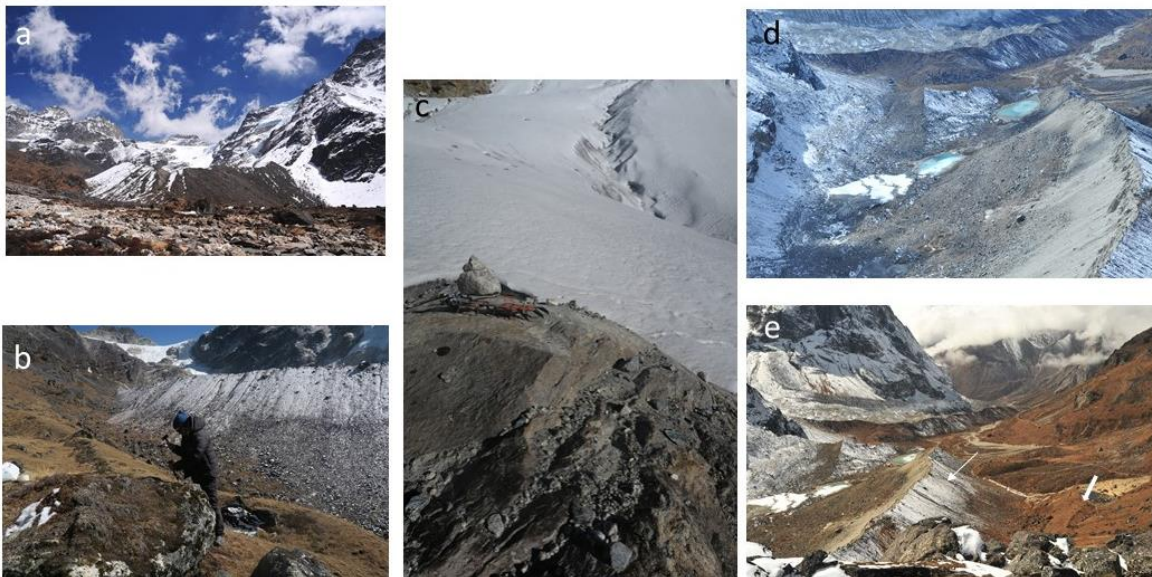


372

373

374 **Figure 2.** Chronology of the Mera glacier's evolution. Geomorphological features are mapped
 375 on aerial imagery of the investigated glacier. White boxes show the ^{10}Be sample ages of moraine
 376 boulders and roches moutonnées with their external uncertainties. Samples written in striked-
 377 through italic text are rejected as outliers and therefore excluded from the discussion. The
 378 weighted mean ages for moraine groups are shown in coloured boxes. **Note that the aerial image**
 379 **used here was taken in the 1990s. ^{10}Be samples from roche moutonnées were collected in 2020**
 380 **at a location which was covered by ice in the 1990s.**

381



382

383 **Figure 3.** Pictures from Mera catchment and moraines. a). Terminal Late Holocene moraine;
 384 b). Sampling on ME-M4 lateral moraine; c). roche moutonnée at the front of the glacier; d).
 385 View from the front of the glacier towards the terminal moraine, note the unstable proximal
 386 slope of the right lateral moraine M1; e). view from the front of the glacier towards the terminal
 387 moraine, note the vegetated lateral right moraine ME-M4 (thick arrow) and the large rampart
 388 composed of ME-M1-3 moraines (fine arrow).

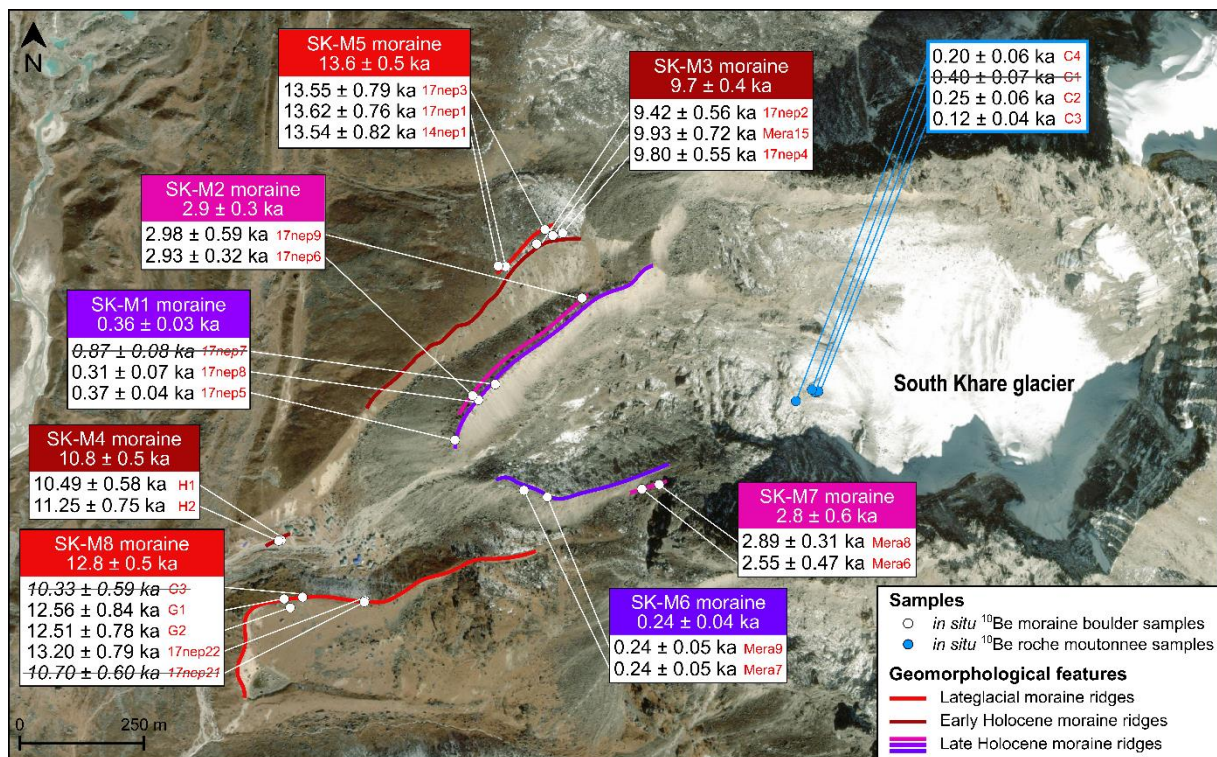
389

390 4-2 South Khare glacier chronology

391 Samples were collected on eight moraine ridges and recently ice-free roches moutonnées close
392 to the front of the glacier (Figs. 4, 5). The four samples (C1, C2, C3 and C4) on these roches
393 moutonnées show apparent ages from 0.12 ± 0.04 ka (C3) to 0.4 ± 0.07 ka (C1). Here again
394 these roches moutonnées were covered by ice until recently suggesting some inheritance related
395 to a complex history of the glacier over at least the Holocene or a reduced thickness of ice over
396 the last centuries.

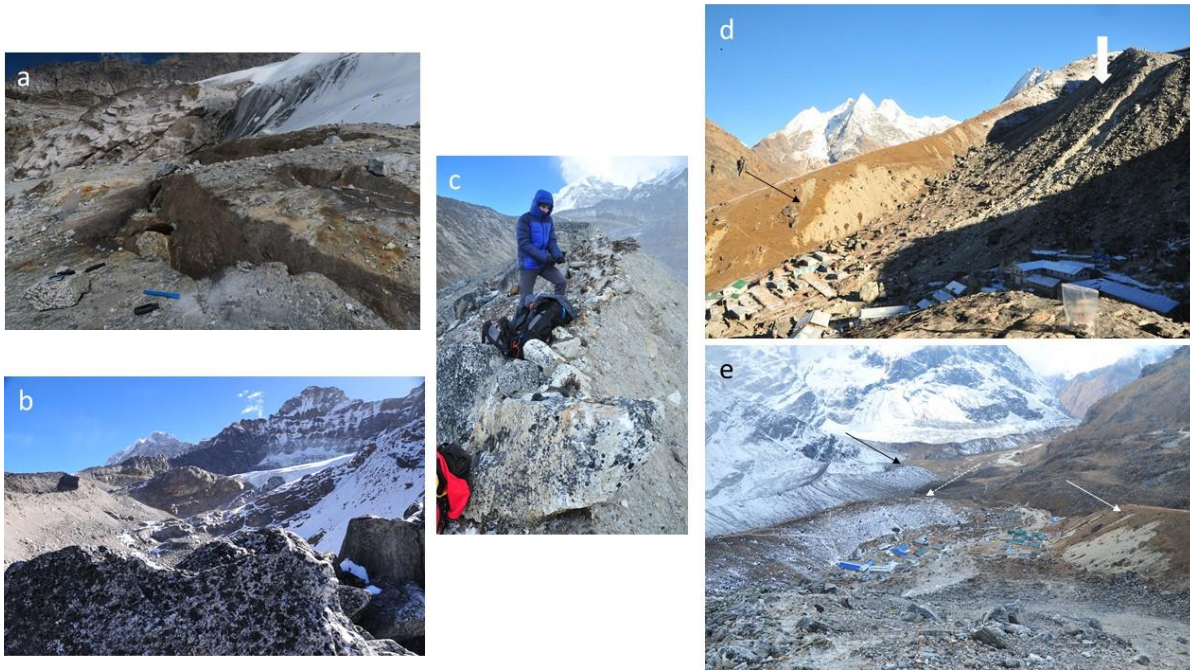
397 On the crest of moraine SK-M1 of South Khare glacier, 3 samples 17nep5, 17nep7, and 17nep8
398 were collected on the uppermost part of the ridge. 17nep7 dated to 0.87 ± 0.08 ka is considered
399 as an outlier based on the χ^2 test and therefore rejected from the mean age calculation of SK-
400 M1, that gives a weighted mean ^{10}Be CRE age of 0.36 ± 0.03 ka. At a distance of about 15 m
401 horizontally from the right lateral moraine on the upper ablation area, another lateral ridge is
402 visible towards the north west of the main valley. This right lateral moraine SK-M2 was dated
403 to 2.9 ± 0.3 ka based on two samples (17nep6 and 17nep9). North of this landform, two nested
404 crests forming the large vegetated moraine located on the right side of the glacier were
405 investigated. On the youngest one three large blocks (1-2 m in length) (17nep2, 17nep4 and
406 Mera15) were selected near the upper ablation zone, where the slope of the longitudinal profile
407 of the moraine is gentle. These samples yield a mean weighted ^{10}Be CRE age of 9.7 ± 0.4 ka. At
408 the base and on the proximal slope of SK-M3 two samples H1 (10.49 ± 0.58 ka) and H2 (11.25
409 ± 0.75 ka) were collected on a remnant ridge of about 100 m long and about 3m in relief. These
410 small blocks (70 -90 cm long) yield a mean ^{10}Be CRE age of 10.8 ± 0.5 ka (SK-M4; n= 2).
411 Assuming this ridge to be connected to the SK-M3 and considering H2 as an outlier (based on
412 the χ^2 test), the moraine ensemble SK-M3 and SK-M4 would give a mean ^{10}Be CRE age of
413 9.9 ± 0.2 ka n=4). Finally, three samples were collected on large boulders (> 1m) on the
414 remnant ridge SK-M5 (14nep1, 17nep1 and 17nep3) which show a weighted mean ^{10}Be CRE
415 age of 13.6 ± 0.5 ka (n=3).

416 On the left side of the glacier two samples were collected on the uppermost ridge SK-M6
 417 (Mera7 and Mera9) that yield a mean ^{10}Be CRE age of 0.24 ± 0.04 ka ($n=2$), which is a bit
 418 younger than the youngest crest SK-M1 on the right size of the glacier. On the distal slope of
 419 the other lateral and discontinuous lateral crest SK-M7 dated to 2.8 ± 0.6 ka ($n=2$) may be
 420 synchronous with SK-M2 on the right side of the glacier (dated to 2.9 ± 0.3 ka). This oldest
 421 lateral SK-M8 moraine on the left side of the glacier was dated to 12.8 ± 0.5 ka based on the
 422 mean of 3 samples (17nep22, G1 and G2).
 423



424
 425 **Figure 4.** Chronology of the South Khare glacier's evolution. Geomorphological features are
 426 mapped on aerial imagery of the investigated glacier. White boxes show the ^{10}Be sample ages
 427 of moraine boulders and roches moutonnées with their external uncertainties. Samples written
 428 in striked-through italic text are rejected as outliers and therefore excluded from the discussion.
 429 The weighted mean ages for moraine groups are shown in coloured boxes.

430
 431



432

433 **Figure 5.** Pictures from South Khare catchment and moraines. a). Roche moutonnée at the base
 434 of the glacier. b). Boulder on the lateral left moraine SK-M6; c). Sampling on SK-M1; d). lateral
 435 view taken from SK-M8, note at the back the vegetated lateral right moraine SK-M3 (black
 436 arrow) and the terminal Late Holocene moraine at the right of the picture (white arrow); e).
 437 picture from the front of the glacier towards the village. Showing the right lateral moraine SK-
 438 M3 (fine white arrow) and SK-M8 (fine dotted white arrow) and a lateral moraine of Mera
 439 glacier black arrow.

440

441 5- Discussion

442 5-1 Evolution of Mera and South Khare glaciers since the Lateglacial

443 The 51 ¹⁰Be CRE ages from samples collected on moraines and roches moutonnées from Mera
 444 and South Khare glaciers in the upper Dudh Koshi basin help addressing questions about the
 445 Lateglacial and Holocene glacier fluctuations and their related climate conditions in the central
 446 Himalaya. The oldest documented moraines are dated to ~13 ka (the two oldest moraines at the
 447 base of South Khare glacier SK-M5 13.6 ± 0.5 ka; SK-M8 12.8 ± 0.5 ka). SK-M5 may have
 448 been formed during the Bølling/Allerød (B/A) (between about 14.7 and 12.9 ka) while SK-M8

449 may have been formed earlier or during the Younger Dryas (YD) (defined between 12.87 ± 0.3
450 and 11.61 ± 0.4 ka; Cheng et al., 2020) on South Khare glacier. Field observations suggest that
451 the glacier experienced an almost comparable extent in the Early Holocene ($11.6 - 8$ ka) as
452 revealed by the existence of the nested moraine SK-M3 (9.7 ± 0.4 ka) on the right side of the
453 glacier against SK-M5 and thus was deposited by a glacier of comparable extent. Since no
454 moraine was dated from the end of the Lateglacial so far on Mera glacier, we speculate that the
455 Early Holocene glacier advance experienced by the glacier is also its oldest moraine record over
456 the investigated period. Thus, the behavior of the two glaciers at the end of the Lateglacial
457 remains elusive and more data are needed to better constrain their evolution during the transition
458 between the warm B/A and the YD.

459 During the Holocene we evidenced that the largest glacial extent occurred in the Early Holocene
460 at $\sim 9-11$ ka on the two glaciers (ME-M4 dated to 11.0 ± 0.3 ka and SK-M3 dated to 9.7 ± 0.4
461 ka). In addition, we did not find any other moraine formed during the Mid-Holocene ($\sim 8-4$ ka)
462 suggesting the extent of the two glaciers was smaller during this period than during the Late
463 Holocene ($\sim 3-0$ ka). Moreover, apparent ages of roche moutonnées recently uncovered by ice
464 showed some inheritance or potential accumulation through the ice that may corroborate this
465 hypothesis. During the Mid-Holocene the front of the glacier would have been located at a
466 higher altitude than the current altitude favouring ^{10}Be accumulation. During the Late Holocene
467 larger glacier advances than during the Mid-Holocene would have eroded earlier pre-exposed
468 bedrock surfaces but not totally removed ^{10}Be accumulated during these previous Mid-Holocene
469 periods free of ice. One may also hypothesize that ^{10}Be might have accumulated when ice
470 thickness was reduced to a few meters due to energetic muon particles (Dunai, 2010). In such
471 a hypothesis the retreat of the glacier during the Mid-Holocene or periods during the Late
472 Holocene could have just been slightly smaller than the latest Late Holocene glacier advances
473 which caused larger extents evidenced by the dated moraines reported in this study. From about

474 3 ka, several advances were recorded with at least two advances larger than those occurring
475 during the Little Ice Age on both glacier's margin (Rowan et al., 2016; Solomina et al., 2016).
476 The oldest one may have occurred at about 2.5 ka as suggested by ME-M5 dated to 2.3 ± 0.2
477 ka on Mera glacier's site, SK-M2 dated to 2.9 ± 0.3 ka and SK-M7 dated to 2.8 ± 0.6 ka on
478 South Khare glacier's site. Another glacier advance period may have occurred at the base of
479 Mera glacier at about 1.5 ka as reported by ME-M3 dated to 1.5 ± 0.2 ka. Finally several
480 advances occurred during the last millennium with ME-M2 dated to 0.8 ± 0.1 ka, and others
481 occurring during the Little Ice Age with SK-M1 dated to 0.36 ± 0.03 ka, ME-M1 dated to 0.3
482 ± 0.03 ka, and SK-M6 Dated to 0.24 ± 0.04 ka.

483

484 Interestingly, the moraines of the investigated glaciers did not vary synchronously at a
485 centennial time scale but revealed a common pattern of change at a millennium time scale. We
486 suspect that these differences in the chronology at a multidecadal time scale may be due to the
487 morphology and topography of the glacier, moraine preservation and uncertainties associated
488 with the CRE ages (Gibbons et al., 1984; Brun et al., 2019). In addition, on the two glaciers,
489 the different extents recorded during the Holocene, in particular during the Late Holocene, have
490 a rather similar amplitude.

491

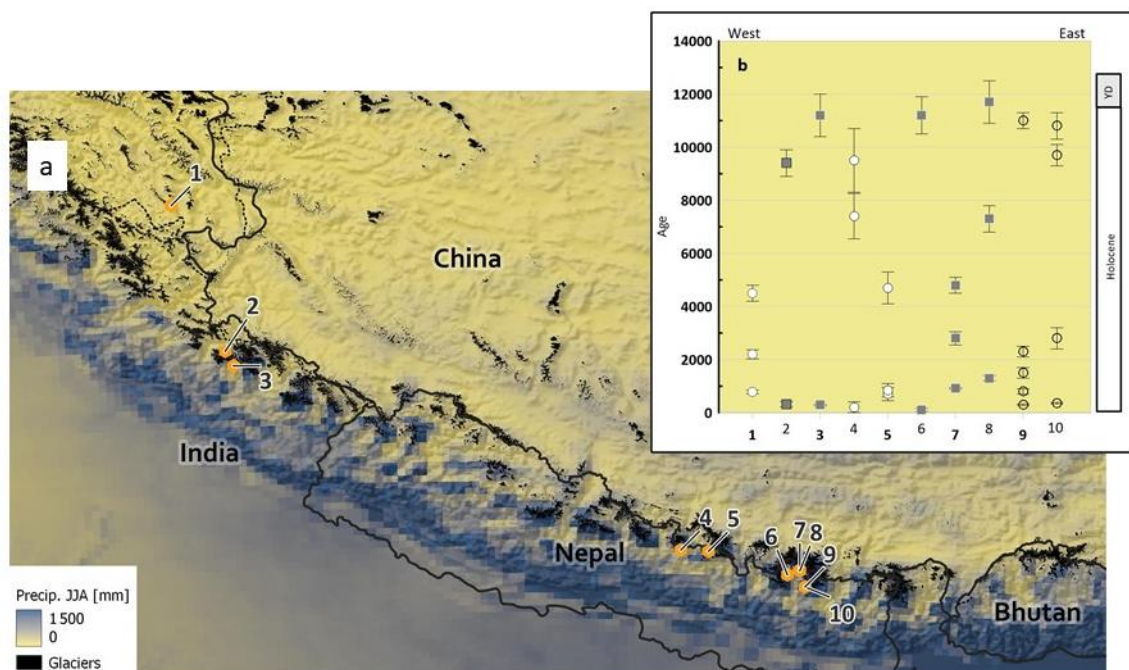
492 5-2 Comparison with other glacier chronologies in Nepal

493 To make easier comparisons, previous chronologies mentioned below were recalculated
494 following the same cosmogenic approach as the one presented in the method section of this
495 paper (production rate, scaling scheme, atmospheric pressure etc). The two small debris-free
496 glaciers investigated in this study revealed intriguing evolution compared with the evolution of
497 another debris-free Paldor glacier located in Ganesh region, central Nepal (Gayer et al., 2006).
498 We notice that the most significant phase of retreat of the debris-free Paldor glacier in Ganesh

499 region (central Nepal), occurred before the Early Holocene (Gayer et al., 2006) (Figs.1, n°5 on
500 fig. 6). This rapid reduction in ice volume was followed by a relative stability of Paldor glacier
501 extent around 11 ka. A second phase of retreat starting soon after 8.5 ka, with a minor readvance
502 during the recent centuries, is suggesting comparable glacier behavior in Ganesh and Everest
503 regions.

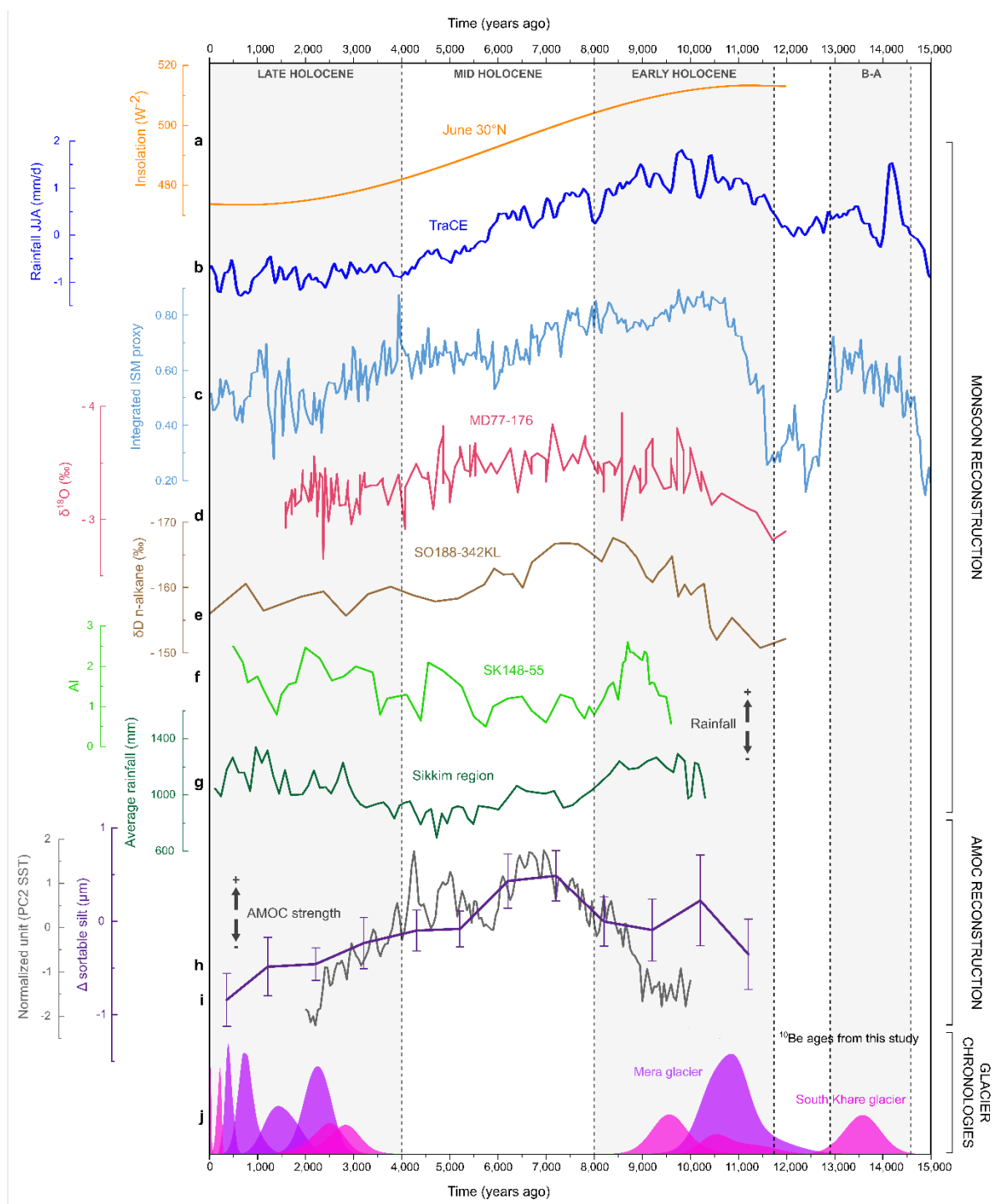
504 On the other hand, in the Khumbu valley, two moraines formed by the debris-covered glacier
505 flowing from Hillary peak in between the Nuptse and Lhotse summits are dated to the Last
506 Glacial Maximum (Finkel et al., 2003) defined between 26.5 ka and 19 ka (Clark et al., 2009)
507 and the Late Holocene respectively. These results show that the maximum Holocene ice extent
508 of this debris-covered glacier occurred during the Late Holocene. This suggests that this glacier
509 would have another pattern of change compared to the debris-covered Khumbu glacier (with a
510 maximum extent dated to ~7 ka) and the two debris-free glaciers investigated in this study.
511 However, more data are needed before being conclusive as undated moraines located in
512 between the Last Glacial Maximum and the Late Holocene exist (this is the reason why we
513 excluded such a case with undated moraines for our comparison). In addition, the age of two
514 moraines downslope from the debris tongue at the base of the northern face of Ama Dablam
515 (Fig. 1; n°7 on Fig.6) investigated by Finkel et al. (2003) reveals that the glacier formed a
516 massive moraine during the YD-Early Holocene transition (~12-11 ka) and another one during
517 the Late Holocene respectively (n°7 on Fig. 6). Thus, the debris-covered tongue of Ama Dablam
518 glacier would show a potentially similar evolution at a millennial time scale with the two
519 debris-free glaciers investigated in this study if one assumes the massive moraine to be formed
520 during the Early Holocene. Finally, the Chhukung stage moraine (defining Early Holocene
521 advance) at the base of the debris-covered Khumbu glacier (n°9 on Fig. 6; Finkel et al., 2003)
522 shows ages from the YD using the same calculation criteria (LSD, VDM, ERA 40 and the same
523 production rate). However, recent investigations on the lateral moraines of Khumbu (n°9 on

524 Fig. 6) suggest a maximum Holocene extent during the Mid-Holocene which is asynchronous
 525 with that of the adjacent Lobuche glacier (n°8 on Fig. 6) occurring during the Late Holocene
 526 (Hornsey et al., 2022). Thus, despite this remarkable pioneer work conducted about 20 years
 527 ago in the Everest region (Finkel et al., 2003) and more recent investigations, it remains difficult
 528 to compare the evolution of debris-free and debris-covered glaciers as more data are needed to
 529 be conclusive. Nevertheless, some moraines of the Late Holocene observed on Mera and South
 530 Khare glaciers were also documented on the two Khumbu and Lobuche glaciers (Hornsey et
 531 al., 2022



532
 533 **Figure 6.** Some glacial chronologies in Himalaya and summer precipitation. a). The
 534 chronologies are plotted on the regional atmospheric High Asia Refined analysis (after Wang
 535 et al., 2020) showing precipitation amount in June, July and August; b). Circle shows a CRE
 536 moraine age with total uncertainty from a debris-free glacier. Rectangle shows a moraine with
 537 total uncertainty from a debris-covered glacier. N°1, Kashmir after Shaha et al. (2019); n°2-3
 538 Garwhal after Barnard et al. (2004) and Murari et al. (2014) respectively; n°4 Ganesh region
 539 (central Nepal) after Gayer et al. (2006); n°5 Langtang Himal after Barnard et al. (2006); n°6-

540 8 Khumbu valley (Nepal) after Finkel et al. (2003) and Hornsey et al. (2022), n°9-10 Mera and
 541 South Kare glaciers this study (see text for further information).



542
 543 **Figure 7.** Nepalese glacier chronologies compared to climate proxies. a). Summer insolation
 544 changes at 30°N; b). precipitation changes (referenced the mean over the whole Holocene)
 545 during the wet season (JJA) from TraCE full forcing experiment (Liu et al., 2009). c). Monsoon

546 reconstruction from a compilation of stalagmite $\delta^{18}O$ from 14 caves (Yu et al., 2022). d).
547 Monsoon reconstruction from marine core MD 177-176 in the Gulf of Bengal after Marzin et
548 al (2013). e). Monsoon reconstruction from SO188-342KL in the Gulf of Bengal after
549 Contreras-Rosales et al. (2014). f). Monsoon reconstruction from sediment core SK 148-55 in
550 Arabian Sea after Thamban et al. (2007). g). Annual precipitation reconstruction from a
551 sediment core in Sikkim region after Ali et al. (2018). h). and i). AMOC reconstructions from
552 Thornalley et al. (2013) and Ayache et al. (2018). j). ^{10}Be CRE age probability density
553 distributions with their analytical uncertainties during the Holocene from mountain glaciers of
554 the investigated Mera (purple shaded curves) and South Khare glaciers. Grey vertical rectangles
555 show major chronozones.

556

557 5-3 Comparison with other glacier chronologies in the HMA

558 Comparing Mera and South Khare glacier chronologies with other glaciers in the HMA does
559 not provide robust conclusions (Finkel et al., 2003; Owen et al., 2009; Saha et al., 2019) .
560 Indeed, glacial chronologies covering the investigated Lateglacial-Holocene period without
561 undated moraine that may have been formed during this time remain very rare ($n < 10$).
562 Moreover, these rare cases do not exhibit a clear regional pattern **whatever the type of glaciers**
563 **considered (debris-free or debris-covered) with a specific glacier evolution in dominated**
564 **westerlies or monsoonal regions. For instance, in Garhwal Himalaya, glaciers from Bhagirathi**
565 **valley (n^o2 Fig. 6, Barnard et al., 2004) may have an in-phase evolution (maximum extent in**
566 **the Early Holocene) with debris-free glaciers reported in this study. However, glaciers in**
567 **Kashmir, or in Langtang Himal (Barnard et al., 2006; Murari et al., 2014; Saha et al., 2018)**
568 **(Figs.1,6), would have another long-term Holocene evolution with a maximum extent**
569 **asynchronous with that reported in this study.** As mentioned earlier, current observations
570 suggest a strong mass balance variability driven by the respective influence of precipitation and

571 temperature on glacier mass balance (Sakaï and Fujita, 2017; Brun et al., 2017). Here we
572 hypothesize that the strong heterogeneity of glacier fluctuations in the past reflects the current
573 heterogeneity of glacier sensitivity to climate conditions as well as the spatial variability of
574 climate change at the scale of the Asian continent.

575

576 5-4 An unresolved relationship between climate forcings and the observed trend of the two
577 debris-free glaciers during the Holocene

578 Multi centennial glacier fluctuations documented by ^{10}Be moraine records reported in this study
579 revealed a possible large glacial extent during the Bølling/Allerød (at the base of SK glacier)
580 and two other large glacier advances, recorded on both glaciers, during the Early and Late
581 Holocene, respectively. The formation of SK-M5 during the B/A corresponds to an enhanced
582 period of precipitations reported by TraCE model and a recent compilation of stalagmite $\delta^{18}\text{O}$
583 data from a total of 14 caves (Yu et al., 2022) spanning 0° – 35°N , 70° – 95°E , that establish a
584 continuous integrated ISM proxy record. However on both records this does not correspond to
585 the maximum of precipitation that occurred during the Early Holocene instead (Fig. 7).
586 Consequently, it remains unclear why SK-M5 is the largest advance while it did not occur
587 during the maximum of precipitation and why we did not observe such an advance on Mera
588 glaciers. Thus we will not further explore possible climate conditions that would explain the
589 formation of this moraine. However, we will discuss the possible climate forcings during the
590 Holocene that may cause the observed large extension during the Early Holocene and the
591 second large advance period occurring in the Late Holocene. For the present-day, the two
592 debris-free glaciers investigated in this study are driven during the wet season on the one hand
593 by precipitation from the Bay of Bengal and on the other hand by temperatures that impact the
594 altitude of the snow/rain phase (Litt et al., 2019; Wagon et al., 2021). We will thus focus

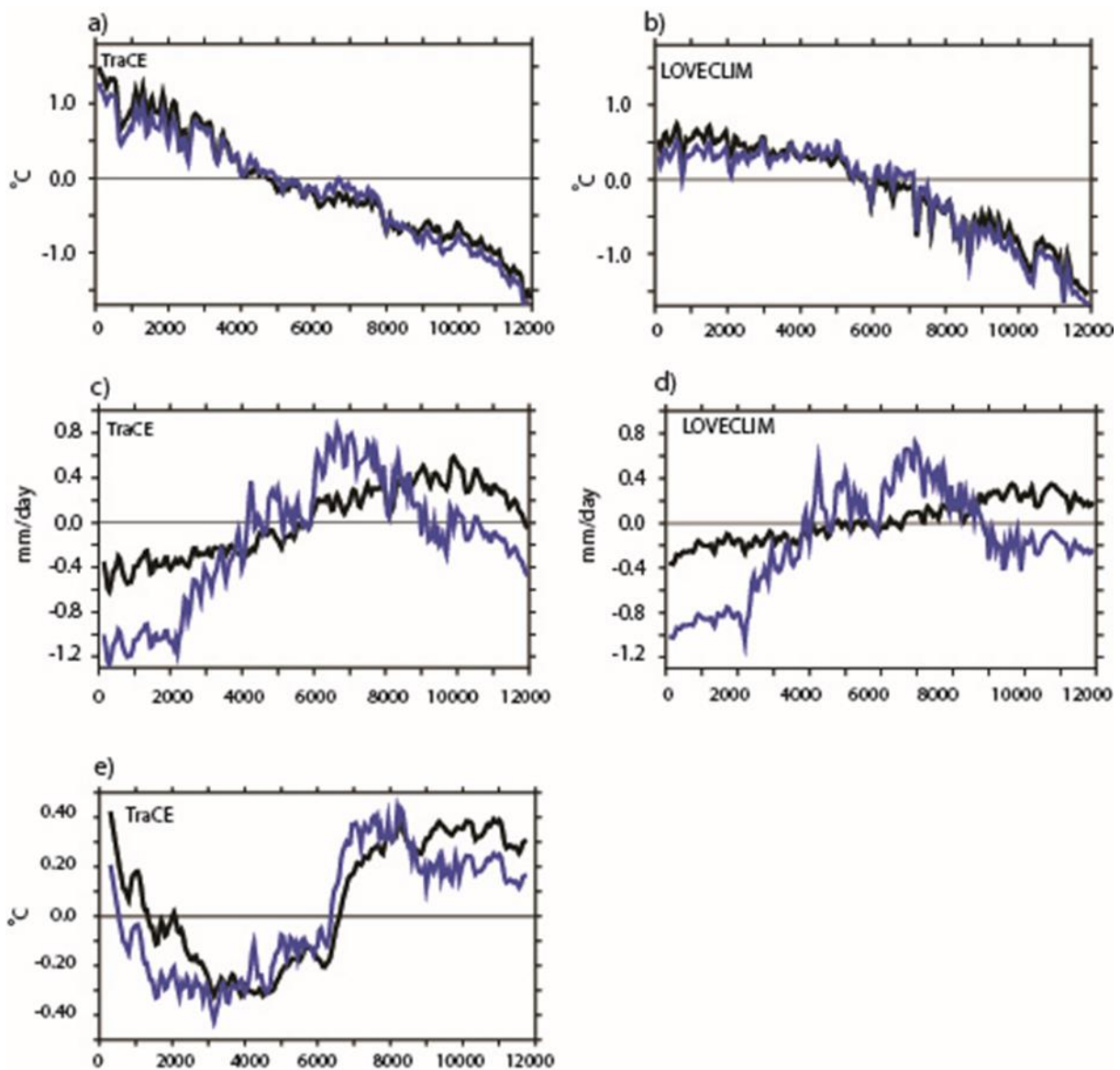
595 successively on these two potential driving factors throughout the Holocene using climate
596 model results and proxy data.

597

598 It is generally considered that a strong ISM occurs during summer insolation maxima and
599 causes enhanced precipitation to the Himalaya (Rachid et al., 2011). By contrast, reduced
600 precipitation related to a weak monsoon occurs during cold periods and weak summer
601 insolation. In a simple way these two large advance periods during the Early and Late Holocene
602 should be explained by an increase in precipitation compared with that during the Mid-
603 Holocene during which these two glaciers are supposed to have retreated.

604 The evolution of precipitation simulated by the full forcing experiments revealed after a
605 maximum in the Early Holocene a progressive decrease throughout the rest of the Holocene
606 (Fig. 7b). None of TraCE and LOVECLIM model simulations show precipitation variations
607 that perfectly fit with the two glacier moraine records investigated in this study. While a
608 maximum ISM in the Early Holocene is concomitant with our moraine records, the simulated
609 evolution of climate conditions during the Mid and Late Holocene cannot simply explain glacier
610 evolution. Causes for this discrepancy can be multiple and might notably be linked to biases in
611 the models. Indeed, from a multi-configuration ensemble of up-to-date fully coupled global
612 transient simulations covering the last 6 ka, Cretat et al (2020) evidenced several model-
613 dependent issues. Tests conducted over the 20th century show that the vegetation–climate
614 interactions modulate the timing of the monsoon onset in the model which can be shifted by
615 more than two months compared to observations. The location of the 2 mm/day isohyet from
616 April to September shows remarkable differences between observations and their simulations.
617 Moreover, differences between observations and their simulations in the variability of monsoon
618 rainfall can exceed 30%. Over the last 6 ka, the drying trend from the Mid-Holocene including
619 extremes, and a contraction of the rainy season evidenced in the IPSL model is larger in

620 simulations with higher horizontal resolution of the atmosphere and improved land surface
621 hydrology. In addition, Mid to Late Holocene changes in JJAS rainfall mean-state documented
622 in the IPSL model show an extraordinary spatial variability with regions where the drying trend
623 is more significant than others.
624
625



626
627 **Figure 8.** Estimates of temperature and precipitation in Mera region from the two GCMs TraCE
628 and LOVECLIM (full forcing experiments). Black line shows the raw data from the two

629 models, the blue line shows AMOC corrected data at an annual time scale, a,b,c,d and e) at a
630 seasonal time scale (JJA). All time series have referenced the mean over the period 2-10 ka BP.

631

632 As precipitation is a key driver of the investigated glaciers, we explore the reconstructions of
633 paleo-precipitation of the ISM to see if they agree with climate model simulations and can
634 explain the glacier evolution. Unfortunately, terrestrial and marine paleo-precipitation records
635 are rare and do not perfectly correlate with model results and moraine records (Rachid et al.,
636 2011). For instance, MD77-176 core located in the Bay of Bengal (14°310 N, 93°080 E, Fig.1)
637 (Marzin et al., 2013) indicates enhanced monsoon rains over the Indian subcontinent between
638 11-8 ka followed by a progressive decrease during the rest of the Holocene (Fig. 7d), in contrast
639 with the general pattern from TraCE simulation (Fig. 7b). A similar pattern of change is shown
640 from a sediment core SO188-342KL (19°.97 N, 90°.03 E; Contreras-Rosales et al., 2014) in the
641 Bay of Bengal.

642 Hypothesizing that the current major source of precipitation falling on Mera glacier from the
643 Bay of Bengal may not be stationary through time (Ali et al., 2018), we thus explored other
644 oceanic and terrestrial monsoon precipitation reconstructions from the Arabian Sea and India
645 respectively (Grupta et al., 2005; Ali et al., 2019; Banerji et al., 2020). However again, none
646 of their results agree with our paleo moraine records (see for instance the sediment core SK148-
647 55 from Thamban et al., 2007 Fig. 7f). Thus, the maximum ISM in the Early Holocene
648 documented both in the composite record of stalagmite $\delta^{18}\text{O}$ data from a total of 14 caves (Fig.
649 7c) (Yu et al., 2022) and in the models agrees with the maximum glacier extent, while there
650 would be a divergence for the rest of the Holocene. In addition, a remarkable exception comes
651 from reconstructed precipitation from a glacial outwash sedimentary profile in Choapta valley,
652 Sikkim Himalaya (located east of the Khumbu region). Here Ali et al. (2018) showed humid
653 periods that roughly match with our moraine records (Fig. 7g). Indeed, the authors identified

654 two periods of unstable climate conditions with higher precipitation during the Early (between
655 10.6-8 ka) and Late Holocene (between 2.9-0.3 ka) respectively, interrupted by dry conditions
656 during the Mid-Holocene. Furthermore, the authors inferred, in agreement with some recent
657 studies (e.g. Sun et al., 2012; Marzin et al., 2013), that the ISM precipitation reconstruction was
658 linked to variations in the North Atlantic climate on multi centennial to millennial time scales,
659 with the AMOC being a potential driver of these changes in North Atlantic climate and its
660 teleconnection with the ISM (e.g. Marzin et al., 2013).

661 As AMOC forcing is known to interact with monsoon (IPCC SROCC 2019), we thus
662 investigated the possible influence of this AMOC forcing on our moraine records. Interestingly,
663 recent reconstruction of AMOC changes revealed two weak AMOC periods during the Early
664 and Late Holocene respectively (Thormaley et al., 2013; Ayache et al., 2018). To further
665 explore this possible influence of AMOC on the ISM and more generally, on the two debris-
666 free glaciers' evolution during the investigated period, we first extracted regional precipitation
667 series at an annual time scale and during the wet season (JJA) from the two full forcing
668 transitory simulations that cover the Holocene simulated by CCSM4 TraCE and LOVECLIM
669 climate models. As AMOC is poorly represented in these two models during the Holocene
670 (Jomelli et al., 2022), we used AMOC reconstructions to compute corrected
671 GCMs precipitation changes over the Holocene according to the method described in Jomelli
672 et al. (2022) (Fig. 8). AMOC corrected monsoon precipitation changes show strong variations
673 with a progressive increase in precipitation culminating during the Mid-Holocene followed by
674 a progressive decrease. Interestingly, these AMOC-corrected precipitation changes (Fig. 8 blue
675 curves) show a good correspondence with precipitation from proxy records in the Bay of Bengal
676 (Fig. 7d, e). This precipitation pattern of the AMOC-corrected precipitation is in line with
677 various modeling results, showing a stronger ISM when the AMOC and the North Atlantic is
678 warmer (e.g. Jackson et al. 2015). However, this pattern does not show a good correspondence

679 with our moraine records since it is going in the opposite directions to what might be required
680 to explain precipitation-driven increase in the glaciers, (i.e. an increase in precipitation).

681

682 Temperature variations would be superimposed on the precipitation evolution. We may also
683 consider that the impact of the two variables (precipitation and temperature) on the glacier
684 would be opposite stronger monsoon (positive influence on mass balance) associated with
685 warmer temperature (negative influence on mass balance) while the influence of temperature
686 could be compensated by an increase in precipitation. However, here again none of TraCE and
687 LOVECLIM model simulations show temperature variations that perfectly fit with the two
688 glacier moraine records investigated in this study (Figs 7, 8).

689

690 All in all, the relationships between climate conditions and long-term glacier changes in the
691 investigated sector of Nepal remain puzzling, and reveal potential issues in the modeling of
692 climate conditions, which could be related to the regional climatic responses in this
693 mountainous region. For instance, due to extreme topography, a large spatial variability of
694 precipitation is currently observed in the central Himalaya, leading to very different
695 precipitation trends over short distances; this is still not captured by models. Moreover, the
696 mass balance sensitivity is highly dependent on the total annual precipitation and therefore may
697 have changed over the Holocene. Finally, the major source of precipitation falling on Mera
698 glacier has potentially changed over time, making it impossible to find a clear relationship
699 between regional climate change and local glacier evolution. To overcome such issues,
700 teleconnections between AMOC and climate conditions in Mera region need further
701 investigations as dynamic downscaling in particular, but this remains beyond the scope of this
702 study. In addition, new moraines chronologies from debris-free glaciers across the mountain

703 range may help to identify a regional trend confirming or negating the evolution of Mera and
704 South Kare glaciers.

705

706 6- Conclusion

707 We documented the evolution of the two debris-free Mera and South Khare glaciers during the
708 end of the Lateglacial and the Holocene in the central Himalaya from 51 cosmogenic ^{10}Be
709 surface exposure ages of samples collected from boulders on moraines and from roche
710 moutonnées. Mera glacier is of particular interest because an energy and mass balance
711 monitoring has been conducted since 2007 enabling a deeper understanding of glacier climate
712 relationships over the recent period. These instrumental measurements indicate that the
713 glaciers' mass balances are driven during the wet summer season (*i*) by precipitation from the
714 Bay of Bengal and (*ii*) by temperatures that impact the altitude of the snow/rain phase.

715 Our paleo glaciological investigations revealed that South Khare glacier evidenced a large
716 glacier extent during the Bølling/Allerød. But glacier advance during this period remains
717 puzzling and new records are needed to better understand climate drivers. On both glaciers ^{10}Be
718 CRE ages also revealed the existence of Early Holocene moraines and attest of their maximum
719 size at that time over the last 11.6 ka. Moreover, the lack of moraine dated to the Mid-Holocene
720 and ^{10}Be inheritance for some roche moutonnées at the base of the current ice front positions
721 suggest the two glaciers were smaller during the Mid-Holocene than during the Late Holocene.
722 From about 3 ka several advances were recorded, which were larger than the LIA.

723 Current observations suggest both glaciers were driven on the one hand by ISM precipitation,
724 and on the other hand by temperature. During the Holocene, these two variables might have
725 been sensitive to summer insolation changes and AMOC changes among other factors. Strong
726 spatial precipitation variability is also evidenced suggesting possible differences between
727 moraine records and proxies or regional precipitation changes estimated from climate

728 models. However, we did not see any ISM precipitation and temperature changes documented
729 from most proxy records and climate model simulations that would perfectly explain the
730 reconstructed glacier changes presented in this study. If the maximum glacial extent is
731 concomitant with enhanced ISM documented from models and some proxy records, the Late
732 Holocene glacier advance remains puzzling. We, therefore, claim that new glacio-
733 geomorphological data combined with improved GCMs output are necessary to get a better
734 understanding of glacier climate relationships in the past in this region.

735

736 Acknowledgments

737 The ASTER AMS national facility (CEREGE, Aix-en-Provence) is supported by the
738 INSU/CNRS, the ANR through the “Projets thématiques d’excellence” program for the
739 “Equipements d’excellence” ASTER-CEREGE action and IRD. Field work, and mass and
740 energy balance results have been supported by the French Service d’Observation
741 GLACIOCLIM, part of IR OZCAR. This work would not have been possible without the
742 support of the IRD International Joint Lab WATER-HIMAL (PIs: D. Shrestha, and P. Wagnon)
743 and all the efforts from people in the field: porters, students, helpers, colleagues who are greatly
744 acknowledged here. T. de Garidel and F. Bassino are also warmly acknowledged for their help
745 with ISM data reconstructions.

746

747 References

748 Ali, S.N., Dubey, J., Ghosh, R., Quamar, M. F., Sharma, A., Morthekai, P., Dimri, A. P.,
749 Shekhar, M., Arif, M., Agrawal. S., 2018. High frequency abrupt shifts in the Indian summer
750 monsoon since Younger Dryas in the Himalaya. *Scientific Reports*, 8(1), 1–8.
751 Ali, S.N., Dubey, J., Shekhar, M., Morthekai, P., 2019. Holocene Indian Summer Monsoon
752 variability from the core monsoon zone of India, a pollen-based review. *Grana* 58, 311-327.

753 Arnold, M., Merchel, S., Bourlès, D. L., Braucher, R., Benedetti, L., Finkel, R.C., Aumaître,
754 G., Gott dang, A., Klein, M., 2010. The French accelerator mass spectrometry facility ASTER:
755 improved performance and developments Nuclear Instrumentation Methods in Physics
756 Research Section B: Beam Interactions with Materials and Atoms 268, 1954–1959.

757 Ayache, M., Swingedouw D., Mary Y., Eynaud F., Colin C., 2018. Multi-centennial variability
758 of the AMOC over the Holocene: A new reconstruction based on multiple proxy-derived SST
759 records. Global and Planetary Change 170, 173-183.

760 Azam, M.F., Kargel, J.S., Shea, J.M., Nepal, S., Haritashya, U.K., Srivastava, S., Maussion, F.,
761 Qazi, N., Chevallier, P., Dimri, A.P., Kulkarni, A.V., Cogley, J.G., Bahuguna, I., 2021.
762 Glaciohydrology of the Himalaya-Karakoram. Science 373 (6557) doi:
763 10.1126/science.abf3668.

764 Balco, G., Stone, J.O., Lifton, N.A., Dunai, T.J., 2008. A complete and easily accessible means
765 of calculating surface exposure ages or erosion rates from ^{10}Be and ^{26}Al measurements. Quat.
766 Geochronol. 3 (3), 174–195.

767 Banerji, U. S., Arulbalaji, P., Padmalal. D., 2020. Holocene climate variability and indian
768 summer monsoon: an overview. The Holocene 30, 766-773.

769 Barnard, P.L. Owen, L.A. Finkel, R.C., 2004. Style and timing of glacial and paraglacial
770 sedimentation in a monsoon-influenced high Himalayan environment, the upper Bhagirathi
771 Valley, Garhwal Himalaya [Sedimentary Geology](#) 165,199-221.

772 Barnard, P.L. Owen, L.A. Finkel, R.C., Asahi. K., 2006. Landscape response to deglaciation in
773 a high relief, monsoon-influenced alpine environment, Langtang Himal, Nepal. Quaternary
774 Science Reviews, 25, 2162-2176.

775 Batbaatar, J., Gillespie, A.R., Fink, D., Matmon, A., Fujioka, T., 2018. Asynchronous
776 glaciations in arid continental climate. Quaternary Science Reviews, 182, 1-19.

777 Bonekamp, P.N.J., de Kok, R.J., Collier, E., Immerzeel, W.W., 2019. Contrasting
778 Meteorological Drivers of the Glacier Mass Balance Between the Karakoram and Central
779 Himalaya. *Front. Earth Sci.* 7:107. doi: 10.3389/feart.2019.00107

780 Bookhagen, B., Burbank, D.W., 2006. Topography, relief and TRMM-derived rainfall
781 variations along the Himalaya. *Geophys. Res. Lett.*, 33, L08405, doi:10.1029/2006GL026037

782 Borchers, B., Marrero, S., Balco, G., Caffee, M., Goehring, B., Lifton, N., Nishiizumi, K.,
783 Phillips, F., Schaefer, J., John Stone, J., 2016. Geological calibration of spallation production
784 rates in the CRONUS-Earth project. *Quat Geochro.* 31, 188-198.

785 Braucher, R., Guillou, V., Bourlès, D. L., Arnold, M., Aumaître, G., Keddadouche, K., Nottoli
786 E., 2015. Preparation of Aster in-house $^{10}\text{Be}/^{9}\text{Be}$ standard solutions. *Nuclear Instruments and*
787 *Methods in Physics Research B*, 361:335–340.

788 Brun, F., Berthier, E., Wagnon, P., Kääb, A., Treichler, D., 2017. A spatially resolved estimate
789 of high mountain Asia glacier mass balances from 2000 to 2016. *Nature Geoscience*, 10:668–
790 673.

791 Brun, F., Wagnon, P., Berthier, E., Jomelli, V., Maharjan, S.B., Shrestha, F. Kraaijenbrink P.
792 D.A., 2019. Heterogeneous influence of glacier morphology on the mass balance variability in
793 high mountain Asia. *Journal of Geophysical Research: Earth Surface*, 121(6):1331–1345.

794 Cheng, H., Zhang, H., Christoph Spötl, C., Baker, J., Sinha, A., Li, H., Bartolomé, M., Moreno,
795 A., Kathayat, G., Zhao, J., Dong, X., Li, Y., Ning, Y., Jia, X., Zong, B., Ait Brahim, Y., Pérez
796 Mejías, C., Cai, Y., Novello, V.F., Cruz, F.W., Severinghaus, J.P., An, Z., Edwards, R.L., 2020.
797 Timing and structure of the Younger Dryas event and its underlying climate dynamics. *PNAS*
798 117, 38. <https://doi.org/10.1073/pnas.200786911>.

799 Chmeleff, J., von Blanckenburg, F., Kossert, K., Jakob, D., 2010. Determination of the ^{10}Be
800 half-life by multicollector ICP-MS and liquid scintillation counting. *Nucl. Instrum. Methods*
801 *Phys. Res., Sect. B* 268 (2), 192–199.

802 Clark, P.U., Dyke, A.S., Shakun, J.D., Carlson, A.E., Clark, J., Wohlfarth, B., Mitrovica, J.X.,
803 Hosteler, S.W., Mc Cabe, A.M., 2009. The last glacial maximum. *Science* 325, 710-714.

804 Contreras-Rosales L.A., Jennerjahn, T., Tharammal, T., Meyer, V., Lückge, A., Paul, A.,
805 Schefus E., 2014. Evolution of the Indian Summer Monsoon and terrestrial vegetation in the
806 Bengal region during the past 18 ka. *Quaternary Sci. Rev.* 102, 133-148.

807 Crétat, J., Braconnot, P., Terray, P., Marti, O., Falasca, F., 2020. Mid-Holocene to present-day
808 evolution of the Indian monsoon in transient global simulations. *Climate Dynamics*, 55, 2761–
809 2784.

810 Dunai, T., 2010. *Cosmogenic Nuclides. Principles, concepts and application in the Earth*
811 *surface Sciences*. Cambridge, 188pp.

812 Finkel, R.C., Owen, L.A., Barnard, P.L., Caffee, M.W., 2003. Beryllium-10 dating of Mount
813 Everest moraines indicates a strong monsoonal influence and glacial synchronicity throughout
814 the Himalaya. *Geology* 31, 561–564.

815 Fugger, S., C. L., Fyffe, C.L., Fatichi, S., Miles, E., McCarthy, M., Shaw, T.E., Ding, B., Yang,
816 W., Wagnon, P., Immerzeel, W., Liu, Q., Pellicciotti, F., 2021. Understanding monsoon control
817 on the mass and energy balance of Himalayan glaciers. *The Cryosphere* 16, 1641-1652.

818 Gayer, E., Lavé, J., Pik, R., France-Lanord, C., 2006. Monsoonal forcing of Holocene glacier
819 fluctuations in Ganesh Himal (Central Nepal) constrained by cosmogenic ³He exposure ages of
820 garnets. 2006. *Earth and Planetary Science Letters* 252, 275–288.

821 Gibbons, A. B., Megeath, J. D., Pierce, K. L., 1984. Probability of moraine survival in a
822 succession of glacial advances. *Geology* 12, 327–330.

823 Gupta, A.K., Das, M., Anderson, D.M., 2005. Solar influence on the Indian summer monsoon
824 during the Holocene. *Geophysical Research Letters*, 32, L17703, doi:10.1029/2005GL022685.

825 Hornsey, J., Rowan, A. V., Kirkbride, M., Livingstone, S.T., Fabel, D., Rodes, A., Quincey,
826 D.J., Hubbard, B., Jomelli, V., 2022. Be-10 dating of ice-marginal moraines in the Khumbu

827 Valley, Nepal, Central Himalaya, reveals the response of monsoon-influenced debris-covered
828 glaciers to Holocene climate change. JGR under review.

829 Hugonnet, R., McNabb, R., Berthier, E., Menounos, B., Nuth, C., Girod, L., Farinotti, D., Huss,
830 M., Dussaillant, I., Brun, F., and Kääb, A., 2021. Accelerated global glacier mass loss in the
831 early twenty-first century. *Nature*, 592, 726-731.

832 Jackson, L. C. Kahana, R., Graham, T., Ringer, M.A., Woollings, T., Mecking, J.V., Wood, R.
833 A., 2015. Global and European climate impacts of a slowdown of the AMOC in a high resolution
834 GCM. *Clim. Dyn.* 45, 3299–3316.

835 Jomelli, V., Francou, B., 2000. Comparing characteristics of rockfall talus and snow avalanche
836 landforms in an alpine environment using a new methodological approach. *Geomorphology*,
837 35, 181-192.

838 Jomelli, V., Swingedouw D., Vuille, M., Favier, V., Goehring, B., Shakun, J., Braucher, R.,
839 Schimmelpfennig I., Menviel, L., Rabatel, A., Martin, L.C.P., Blard, P-H., Condom, T., Lupker,
840 M., Christl, M., He, Verfaillie, D., Z., Gorin, A., ASTER Team. 2022. AMOC control on
841 millennial-scale glacier changes during the Holocene. *Nature com*, doi.org/10.1038/s41467-
842 022-28939-9

843 Kaufman, D., and 102 others 2020. A global database of Holocene paleo temperature records.
844 *Scientific Data* 7, 115, <https://doi.org/10.1038/s41597-020-0445-3>.

845 Khadka A, Wagnon, P., Shrestha, D., Brun, F., Koch, I., 2022 Validation of ERA5 Land Data
846 in the Upper Dudh-Koshi Region and its implication for Energy/Mass balance, *J. Applied*
847 *Meteo.*, 61(8)DOI: 10.1175/JAMC-D-21-0091.1

848 Kobashi, T., Menviel, L., Jeltsch-Thömmes, A., Vinther, B. M., Box, J. E., Muscheler, R.,
849 Nakaegawa, T., Pfister, P. L., Döring, M., Leuenberger, M., Wanner, H., Ohmura, A., 2017:
850 Volcanic influence on centennial to millennial Holocene Greenland temperature change.
851 *Scientific Reports* 8, 1, 4292.

852 Korschinek, G., Bergmaier, A., Faestermann, T., Gerstmann, U.C., Knie, K., Rugel, G.,
853 Wallner, A., Dillmann, I., Dollinger, G., von Gostomski, Ch.L., Kossert, K., Maiti, M.,
854 Poutivtsev, M., Remmert, A., 2010. A new value for the half-life of ^{10}Be by Heavy-Ion Elastic
855 Recoil Detection and liquid scintillation counting. Nuclear Instruments and Methods in Physics
856 Research Section B: Beam Interactions with Materials and Atoms 268, 2, 187–191:
857 doi:10.1016/j.nimb.2009.09.020.

858 Lal, D., 1991. Cosmic ray labeling of erosion surfaces: *in situ* nuclide production rates and
859 erosion models. Earth and Planetary Science Letters 104, 2–4, 424–439: doi:10.1016/0012-
860 821X(91)90220-C.

861 Lifton, N., Sato, T., Dunai, T.J., 2014. Scaling in situ cosmogenic nuclide production rates using
862 analytical approximations to atmospheric cosmic-ray fluxes. Earth Planet. Sci. Lett. 386, 149–
863 160. <https://doi.org/10.1016/j.epsl.2013.10.052>.

864 Litt, M., Shea, J., Wagnon, P., Steiner, J. Koch, I. Stigter, E., Immerzeel. W., 2019. Glacier
865 ablation and temperature indexed melt models in the nepalese himalaya. Scientific Reports,
866 9(1).1–10.

867 Liu, Z., Otto-Bliesner, B.L., Hee, F., Brady, E.C. Tomas, R., Clark, P.U., Carlson, A.E., Lynch-
868 Steiglitz, J., Curry, W., Brook, E., Erickson, D., Jacob, R., Kutzbach, J., Cheng, J., 2009.
869 Transient simulation of deglacial Climate Evolution with a new mechanism for Bolling-Allerod
870 warming. Science 325, 310-314.

871 Martin, L. C. P., Blard, P.-H., Balco, G., Lave, J., Delunel, R., Lifton, N., Laurent, V., 2017.
872 The CREp program and the ICE-D production rate calibration database: a fully parameterizable
873 and updated online tool to compute cosmic-ray exposure ages. Quaternary Geochronology 38,
874 25–49.

875 Marzin, C., Kallel, N., Kageyama, M., Duplessy, J. C., Braconnot, P., 2013. Glacial of the Indian
876 monsoon and their relationship with North Atlantic climate: New data and fluctuations and
877 modelling experiments. *Climate of the Past* 9, 2135–2151.

878 Matthews, T., Perry, L. B., Koch, I., Aryal, D., Khadka, A., Shrestha, D., Abernathy, K., Elmore,
879 A. C., Seimon, A., Tait, A., Elvin, S., Tuladhar, S., Baidya, S. K., Potocki, M., Birkel, S.
880 D., Kang, S., Sherpa, T. C., Gajurel, A., Mayewski, P. A., 2020. Going to Extremes: Installing
881 the World's Highest Weather Stations on Mount Everest, *B. Am. Meteorol. Soc.*, 101, E1870–
882 E1890, <https://doi.org/10.1175/BAMS-D-19-0198.1>, 2020.

883 McKay, N.P., Kaufman D.S., Routsos C.C., Erb M.P., Zander P.D., 2018. The Onset and Rate
884 of Holocene Neoglacial Cooling in the Arctic. *GRL* 45, doi.org/10.1029/2018GL079773

885 Merchel, S., Bremser, W., Alfimov, V., Arnold, M., Aumaître, G., Benedetti, L., Bourles, D.L.,
886 Caffee, M., Fifield, L.K., Finkel, R.C., Freeman, S.P.H.T., Martschini, M., Matsushi, Y., Rood,
887 D.H., Sasa, K., Steier, P., Takahashi, T., Tamari, M., Tims, S.G., Tosaki, Y., Wilcken, K.M.,
888 Xu, S., 2011. Ultra-trace analysis of ^{36}Cl by accelerator mass spectrometry: an interlaboratory
889 study. *Anal. Bioanal. Chem. Res.* 400, 3125–3132.

890 Mölg, T., Maussion, F., Scherer, D., 2014. Mid-latitude westerlies as a driver of glacier
891 variability in monsoonal High Asia. *Nat. Clim. Change* 4, 68–73.

892 Murari, M.K., Owen, L.A., Dortch, J.M., Caffee, M.W., Dietsch, C., Fuchs, M., Haneberg,
893 W.C., Sharma, M.C., Townsend-Small, A., 2014. Timing and climatic drivers for glaciation
894 across monsoon-influenced regions of the Himalayan–Tibetan orogen. *Quaternary Sci. Rev.*
895 88, 159–182.

896 Owen, L.A., 2009. Latest Pleistocene and Holocene glacier fluctuations in the Himalaya and
897 Tibet. *Quaternary Sci. Rev.* 28, 2150–2164.

898 Owen, L.A., Finkel, R.C., Barnard, P.L., Haizhou, M., Asahi, K., Caffee, M.W., Derbyshire,
899 E., 2005. Climatic and topographic controls on the style and timing of Late Quaternary

900 glaciation throughout Tibet and the Himalaya defined by ^{10}Be cosmogenic radionuclide
901 surface exposure dating. *Quaternary Sci. Rev.* 24, 1391–1411.

902 Owen, L.A., Caffee, M.W., Finkel, R.C., Seong, B.Y., 2008. Quaternary glaciations of the
903 Himalayan–Tibetan orogen. *Journal of Quaternary Science* 23, 513–532.

904 Owen, L.A., Robinson, R., Benn, D.I., Finkel, R.C., Davis, N.K., Yi, C., Putkonen, J., Li, D.,
905 Murray, A.S., 2009. Quaternary glaciation of Mount Everest. *Quaternary Sci. Rev.* 28, 1412–
906 1433.

907 Owen, L.A., Dortch, J.M., 2014. Nature and timing of Quaternary glaciation in the Himalayan–
908 Tibetan orogen. *Quaternary Sci. Rev.* 88, 14–54.

909 Perry, L. B., Matthews, T., Guy, H., Koch, I., Khadka, A., Elmore, A.C., Shrestha, D.,
910 Tuladhar, S., Baidya, S.K., Maharjan S., Wagnon, P., Aryal, D., Seimon, A., Gajurel, A.,
911 Mayewski, P. A., 2020. Precipitation characteristics and moisture source regions on Mt. Everest
912 in the Khumbu, Nepal. *One Earth* 3, 594–607.

913 Pritchard, H. D., 2019. Asia’s shrinking glaciers protect large populations from drought stress.
914 *Nature* 569, 649–654.

915 Rashid, H., England, E., Thompson, L Polyak L., 2011. Late glacial to holocene indian summer
916 monsoon variability based upon sediment records taken from the bay of bengal. *Terrestrial,*
917 *Atmospheric and Oceanic Sciences*, 22, 215–228.

918 Rowan, A. V., 2016. The ‘Little Ice Age’ in the Himalaya: a review of glacier advance driven
919 by Northern Hemisphere temperature change. *The Holocene* 27, 292–308.

920 Rowan, A.V., Egholm, D.L., Quincey, D.J., Glasser, N.F., 2015. Modelling the feedbacks
921 between mass balance, ice flow and debris transport to predict the response to climate change
922 of debris covered glaciers in the Himalaya. *Earth and Planetary Science Letters* 430, 427–438.
923 <https://doi.org/10.1016/j.epsl.2015.09.004>

924 Saha, S., Owen, L.A. Orr, E.N., Caffee. M.W., 2018. Timing and nature of holocene glacier
925 advances at the northwestern end of the himalayan-tibetan orogen. *Quaternary Sci. Rev.*
926 187,177–202,

927 Saha, S., Owen, L.A. Orr, E.N., Caffee. M.W., 2019. Cosmogenic ¹⁰be and equilibrium-line
928 altitude dataset of holocene glacier advances in the himalayan-tibetan orogen. *Data in Brief*,
929 26:104412. <https://doi.org/10.1016/j.dib.2019.104412>

930 Saha, S., Owen, L.A., Orr, E.N., Caffee M.W., 2019. High-frequency Holocene glacier
931 fluctuations in the Himalayan Tibetan orogen. *Quaternary Sci. Rev.* 220, 372-400.

932 Sakaï, A., Fujita, K., 2017. Contrasting glacier responses to recent climate change in high
933 mountain Asia. *Scientific Reports* 7, 13717 | DOI:10.1038/s41598-017-14256-5

934 Sherpa, S. F., Wagnon, P., Brun, F., Berthier, E., Vincent, C., Lejeune, Y., Arnaud, Y.,
935 Kayastha, R., Sinisalo, A., 2017. Contrasted surface mass balances of debris-free glaciers
936 observed between the southern and the inner parts of the Everest region (2007-2015). *J. Glaciol*,
937 doi: 10.1017/jog.2017.30

938 Seong, Y.B., Owen, L.A., Bishop, M.P., Bush, A., Clendon, P., Copland, L., Finkelf, R., Kamp,
939 U., Shroder Jr., J.F., 2007. Quaternary glacial history of the Central Karakoram. *Quaternary*
940 *Sci. Rev* 26, 3384–3405.

941 Stigter, E.E., Litt, M., Steiner, J.F., Bonekamp, P.N.J., Shea, J.M., Bierkens, M.F.P.,
942 Immerzeel, W.W., 2018. The Importance of Snow Sublimation on a Himalayan Glacier. *Front.*
943 *Earth Sci.* 6:108. doi: 10.3389/feart.2018.00108

944 Stigter, E.E., Steiner, J.F., Koch, I., Saloranta, T.M., Kirkham, J.D., Immerzeel, W.W., 2021.
945 Energy and mass balance dynamics of the seasonal snowpack at two high-altitude sites in the
946 Himalaya. *Cold Regions Science and Technology*,183,103233, ISSN 0165-232X,
947 <https://doi.org/10.1016/j.coldregions.2021.103233>.

948 Solomina, O.N., Bradley, R.S., Hodgson, D.A., Ivy-Ochs, S., Jomelli, V., Mackintosh, A.N.,
949 Nesje, A., Owen, L.A., Wanner, H., Wiles, G.C., Young, N.E., 2015. Holocene glacier
950 fluctuations. *Quaternary Sci. Rev.* 111, 9–34.

951 Solomina, O., Bradley., Jomelli, V., Geirsdottir, A., Kaufman, D., Koch, J., Masiokas, M.,
952 Miller, G., Nesje, A., Nicolussi, K., Owen, L., Wanner, H., Wiles, G., Yang, B., 2016. Glacier
953 fluctuations in the last 2000 years. *Quaternary Sci. Rev.* 149, 61-90.

954 Sun, Y. Clemens, S.C., Morrill, C., Lin, X., Wang, X., An, Z., 2012. Influence of Atlantic
955 meridional overturning circulation on the East Asian winter monsoon: *Nature Geoscience* 5,
956 46–49.

957 Stone, J.O., 2000. Air pressure and cosmogenic isotope production. *Journal of Geophysical*
958 *Research: Solid Earth* 105, B10, 23753–23759: doi:10.1029/2000JB900181.

959 Swingedouw, D., Rodehacke, C.B., Behrens, E., Menary, M., Olsen, S.M., Gao, Y.,
960 Mikolajewicz, U., Mignot, J., Biastoch, A., 2013. Decadal fingerprints of freshwater discharge
961 around Greenland in a multi-model ensemble. *Clim. Dyn.* 41, 695–720.

962 Thamban, M., Kawahata, H., Purnachandra Rao, V., 2007. Indian Summer Monsoon
963 Variability during the Holocene as Recorded in Sediments of the Arabian Sea: Timing and
964 Implications. *Journal of Oceanography* 63, 1009-1020.

965 Thornalley, D. J. R., Blaschek, M., Davies, F. J., Praetorius, S., Oppo, D. W., McManus, J. F.,
966 Hall, I. R., Kleiven, H., Renssen, H., McCave, I.N., 2013. Long-term variations in Iceland–
967 Scotland overflow strength during the Holocene *Geoscientific Instrumentation Methods and*
968 *Data Systems* long-term variations in Iceland–Scotland overflow strength during the Holocene.
969 *Clim. Past* 9, 2073–2084.

970 Upasana, S.B., Arulbalaji, P., Padmalal, D., 2020. Holocene climate variability and Indian
971 Summer Monsoon: An overview. *The Holocene* 30,744–773

972 Uppala, S.M., Kållberg, P.W., Simmons, A.J., Andrae, U., Bechtold, V.D.C., Fiorino, M.,
973 Gibson, J.K., Haseler, J., Hernandez, A., Kelly, G.A., Li, X., Onogi, K., Saarinen, S., Sokka,
974 N., Allan, R.P., Andersson, E., Arpe, K., Balmaseda, M.A., Beljaars, A.C.M., Berg, L.V.D.,
975 Bidlot, J., Bormann, N., Caires, S., Chevallier, F., Dethof, A., Dragosavac, M., Fisher, M.,
976 Fuentes, M., Hagemann, S., Hólm, E., Hoskins, B.J., Isaksen, L., Janssen, P.A.E.M., Jenne, R.,
977 McNally, A.P., Mahfouf, J.-F., Morcrette, J.-J., Rayner, N.A., Saunders, R.W., Simon, P., Sterl,
978 A., Trenberth, K.E., Untch, A., Vasiljevic, D., Viterbo, P., Woollen, J., (2005). The ERA-40
979 re-analysis. *Q.J.R. Meteorol. Soc.*, 131, 2961-3012.

980 Wagon, P., Vincent, C. Arnaud, Y. Berthier, E. Vuillermoz, E. Gruber, S. Ménégoz, M.
981 Gilbert, A. Dumont, M., Shea, J. M. Stumm, D., Pokhrel. B. K., 2013. Seasonal and annual mass
982 balances of Mera and Pokalde glaciers (Nepal Himalaya) since 2007. *Cryosphere*, 7(6):1769–
983 1786, 2013.

984 Wagon, P., Brun, F., A. Khadka, A. Berthier, E. Shrestha, D. Vincent, C. Arnaud, Y. Six, D.
985 Dehecq, A. Ménégoz, M., Jomelli. V., 2021. Reanalysing the 2007–19 glaciological mass-
986 balance series of mera glacier, Nepal, central Himalaya, using geodetic mass balance. *Journal*
987 *of Glaciology* 67,117–125.

988 Wang, X., Tolksdorf, V., Otto, M., Scherer, D., 2020. WRF-based dynamical downscaling of
989 ERA5 reanalysis data for High Mountain Asia: Towards a new version of the High Asia Refined
990 analysis. *International Journal of Climatology*, 41, 742-763. <https://doi.org/10.1002/joc.6686>

991 Ward G. K., Wilson. S. R., 1978. Procedures for comparing and combining radiocarbon age
992 determinations: a critique. *Archaeometry* 20,19–31.

993 Yan, Q., Owen, L.A., Zhang, Z., Jiang, N., Zhang, R., 2020. Deciphering the evolution and
994 forcing mechanisms of glaciation over the Himalayan-Tibetan orogen during the past 20,000
995 years. *EPSL*, 541, DOI: 10.1016/j.epsl.2020.116295

996 Yu, Z., Colin, C., Wilson, D. J., Bayon, G., Song, Z., Sepulcre, S., Dapoigny, A., Li, Y., Wan,
997 S., 2022. Millennial variability in intermediate ocean circulation and Indian monsoonal
998 weathering inputs during the last deglaciation and Holocene. *Geophysical Research Letters*, 49,
999 e2022GL100003. <https://doi.org/10.1029/2022GL100003>

1000

1001 Tables

1002

1003 Table 1. Cosmogenic data from Mera and South Khare glaciers. The mean age of the landforms
1004 is calculated with external uncertainties.

1005 Table 2. Cosmogenic ages calculated using different model schemes. Scaling to the sample
1006 locations was made according to the recent, physically-based, LSD model (Lifton et al., 2014)
1007 which performs similarly to older empirical models (Borchers et al., 2016). Chosen parameters
1008 include the ERA 40 atmospheric reanalysis (Uppala et al., 2005) and the VDM 2016
1009 geomagnetic database.

1010

Competing interests

The authors declare no competing interests

Author contributions

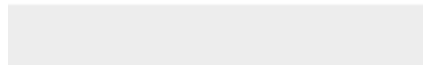
V.J. designed the paper. V.J., P.W., F.B., and D.S. realized the field Sampling R.B., J.C., A.H., S.B and V.J. processed the ^{10}Be sample preparation and analysis. V.J., R.B., J.C., A.H., S.B and ASTER TEAM computed the cosmogenic nuclides ages. D.S. ran the AMOC simulations. V.J., D.S., and P.W. analyzed forcings. V.J. wrote the first draft of the paper and all authors contributed to the discussion and final version of the manuscript.




Click here to access/download

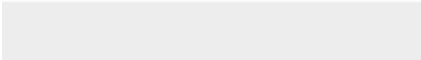

e-Component/Supplementary data

1TABLE_S1 16_12Outlier-Batbaatar way.xlsx



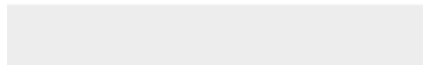


Click here to access/download
e-Component/Supplementary data
figure Sup1.jpg





Click here to access/download
e-Component/Supplementary data
figureSup2.jpg





Click here to access/download
e-Component/Supplementary data
figureSup3.jpg

